The impact of grain size on the hydromechanical behavior of mudstones

Julia S. Reece

Department of Geology and Geophysics, Texas A&M University, College Station, Texas, USA

Corresponding author: Julia S. Reece (jreece@geos.tamu.edu)

Key Points:

- Mudstone compressibility decreases and vertical permeability increases with decreasing clay fraction
- I apply empirical models to predict compression and permeability behavior in mudstone – silt mixtures
- Increasing creep with depth and different fabrics explain differences in compression curves of field, intact, and resedimented samples

Abstract

Porosity and compression index systematically decrease and permeability systematically increases with decreasing clay fraction over vertical effective stresses ranging from 0 – 21 MPa in reconstituted mudstones from offshore Japan. I use six sediment mixtures composed of varying proportions of hemipelagic mudstone and silt-size silica resulting in clay fractions ranging from 56% to 32% by mass. The hemipelagic mudstone is from Site C0011 drilled seaward of the Nankai Trough, offshore Japan, during Integrated Ocean Drilling Program Expedition 322. Uniaxial resedimentation and constant rate of strain consolidation experiments on these sediment mixtures illuminate how the compression and permeability behavior vary as a function of clay fraction and stress. Backscattered electron microscope images show that as compressible clay particles with small, elongated, and crescent-shaped pores are being replaced by solid quartz grains, the matrix porosity declines and large, jagged pore throats between silt grains are preserved in compaction shadows. This results in reduced compressibilities and increased permeabilities. I compare the behavior of reconstituted samples with that of intact core and field measurements and provide empirical compression and permeability models that describe the evolution of porosity (void ratio) and permeability with vertical effective stress and as a function of grain size. Characterizing the in situ hydromechanical properties of subduction inputs is critical in order to relate input sediments to those at frontal thrust regions and understand the mechanics of accretionary prisms, plate boundary earthquakes, and fault slip behavior at subduction zones.

Plain Language Summary

Sediments containing significant amounts of clay are widespread on our planet, especially beneath the seafloor. The rate at which the porosity (volume of pore space between the grains) and permeability (ease with which fluid flows through sediments) decrease during burial is impacted by the clay fraction. These properties are critical in predicting pressures and stresses in the subsurface and understanding earthquake generation in Earth's collisional continental margins. Based on laboratory experiments and microscale imaging of systematically prepared sediment mixtures, I show that the less clay a sediment contains the stiffer it becomes and the easier it is for fluid to flow through. I provide models to predict porosity and permeability for

varying clay fractions as a function of increasing stress/depth. This study uses sediments from the Nankai margin, offshore southwest Japan, one of the great collisional zones in the world.

Index Terms and Keywords

Index Terms: 3021 Marine hydrogeology, 3036 Ocean drilling, 3060 Subduction zone processes, 5114 Permeability and porosity, 5112 Microstructure

Keywords: Integrated Ocean Drilling Program, sediment mixtures, compressibility, permeability, clay fraction, overconsolidation

1 Introduction

Mudstones are fine-grained sediments containing clay- and silt-size particles, and compose nearly 60-70% of the volume of sedimentary basins (Dewhurst et al., 1998; Yang and Aplin, 2010). Their consolidation behavior differs significantly from that of coarser sediments because of their low permeability and high compressibility. This affects a series of natural and human induced processes. Specifically, the consolidation behavior of mudstones controls fluid pressures and effective stresses in the subsurface (Gibson, 1958; Green & Wang, 1986) and has important implications for fluid migration including water, petroleum, and CO_2 (Bethke, 1989; Dugan & Flemings, 2000), development of overpressure (Broichhausen et al., 2005; Flemings et al., 2008; Long et al., 2011; Schneider et al., 2009), generation of landslides (Dugan & Flemings, 2000), formation of mud diapirs (Graue, 2000; Milkov, 2000), and the entrapment of petroleum (England et al., 1987; Schlömer & Krooss, 1997) or radioactive waste and CO_2 (Bickle et al., 2007; Holloway, 2001; Huysmans & Dassargues, 2006; Marty et al., 2003).

In accretionary wedge systems like the Nankai subduction zone, the mechanical and hydrological properties of sediments on the incoming sea plate, which are mostly marine mudstones, control in situ effective stress and pore pressure within the accretionary prism. Pore fluid pressure affects a wide range of important deformation and fluid transport processes through its control on effective normal stress (Saffer & Tobin, 2011), including absolute strength of faults and prism sediments (e.g., Davis et al., 1983; Hubbert & Rubey, 1959), accretionary wedge geometry (Davis et al., 1983), and the occurrence of earthquakes (e.g., Dixon & Moore, 2007; Scholz, 1998) and fault slip behaviors like slow slip events, very low-frequency

earthquakes, and episodic tremor and slip (e.g., Audet et al., 2009; Kitajima & Saffer, 2012; Liu & Rice, 2007; Obana & Kodaira, 2009). In fact, pore fluid pressures in accretionary prisms reflect a dynamic balance between geologic forcing and fluid escape (Saffer & Tobin, 2011). At many subduction margins, including Nankai subduction zone, pore pressures support between 70% and 95% of the overburden (e.g., Bekins et al., 1995; Davis et al., 1983; Ellis et al., 2015; Flemings & Saffer, 2018; Saffer & Bekins, 1998, 2006; Suppe, 2007; Wang, 1994). Rapid tectonic loading on unconsolidated sediment is often considered the most important factor that contributes to the overpressure generation (Kitajima & Saffer, 2012; Saffer & Tobin, 2011).

Variations in sediment composition and clay content from one margin to the next and along strike of individual margins (Underwood, 2007) affect fluid budgets (Saffer & Tobin, 2011) and hydromechanical behavior of sediments, which in turn controls the pore fluid pressure distribution in the accretionary prism. For example, low-permeability, high-compressibility incoming sediments will limit fluid drainage, thus preserve high overpressure (e.g., Barker et al., 2009; Saffer & Bekins, 2002), while highly porous and permeable incoming sediments with low-compressibility result in better-drained conditions associated with lower pore pressure (e.g., Barker et al., 2009; Lallemand et al., 1994; Saffer & Tobin, 2011). Therefore, it is imperative to systematically study the impact of composition and grain size on mechanical and hydrological properties of the sediments that are being deposited on the incoming sea plate and undergo uniaxial (vertical) consolidation in front of the accretionary prism, before they either continue uniaxial burial beneath the décollement or experience increasing horizontal stresses within the wedge until the material fails.

Mechanical compression of mudstones is defined as the porosity loss as a function of effective stress and is controlled by many factors including grain size and shape, previous stress history, sedimentation rate, temperature, clay mineralogy, and presence of organic matter (e.g., Bennett et al., 1991; Collins & McGown, 1974). The compression behavior is commonly measured in the laboratory using consolidation experiments such as uniaxial incremental oedometer tests (e.g., Hüpers & Kopf, 2012; Kitajima & Saffer, 2014; Mondol et al., 2007) or constant rate of strain consolidation tests (e.g., Casey et al., 2019; Guo & Underwood, 2014; Kitajima & Saffer, 2014; Long et al., 2011; Reece et al., 2013). Various empirical models exist to describe the one-dimensional compression behavior of mudstones during normal compression: a log-linear relationship between effective stress and void ratio (Burland, 1990; Lambe &

Whitman, 1969; Skempton & Jones, 1944) or porosity (Karig & Ask, 2003), a log-log relationship between effective stress and specific volume (Baldwin & Butler, 1985; Butterfield, 1979; Long et al., 2011), or an exponential relationship between effective stress and porosity (Athy, 1930; Rubey & Hubbert, 1959). But no one model can describe the behavior of all sediment types. In fact, Casey et al. (2019) showed based on their study of 15 different mudstones that, when mudstones are divided into either silt-rich, low liquid limit sediments or smectite-rich, high liquid limit sediments, log-linear relationships between vertical effective stress and void ratio or porosity, respectively, best describe the one-dimensional compression behavior.

Mudstone permeability varies across orders of magnitudes and is controlled by porosity, grain size, pore size distribution, grain shape, tortuosity, and temperature (e.g., Carman, 1937; Kozeny, 1927; Scheidegger, 1974; Spinelli et al., 2004). Vertical permeability is commonly measured using steady-state flow-through experiments (e.g., Dugan & Zhan, 2013) or transient pulse decay tests (e.g., Yang & Aplin, 2007), or derived from constant rate of strain (CRS) consolidation tests (e.g., Guo & Underwood, 2014; Kitajima & Saffer, 2014; Reece et al., 2012; Reece et al., 2013) or incremental loading tests (e.g., Hüpers & Kopf, 2012; Kitajima & Saffer, 2014). But measurements of permeability are often complicated and require large sample sizes. Therefore, in more recent years, vertical permeability has also been estimated from liquid limit (Casey et al., 2013) and nuclear magnetic resonance (NMR) data (Daigle & Dugan, 2009). The evolution of permeability during burial is most commonly modelled with a log-linear relationship between permeability and porosity. Several empirical models of this type of relationship exist for various lithologies, including along the Japan trench (e.g., Gamage & Screaton, 2006; Gamage et al., 2011; Kitajima & Saffer, 2014; Saffer & Bekins, 1998; Screaton & Ge, 2012; Skarbek & Saffer, 2009).

Both the compression and permeability relationships have been long known to be strongly influenced by lithology (Aplin et al., 1995; Burland, 1990; Skempton, 1970; Tavenas et al., 1983), often expressed as grain size or clay content. For example, the wide range in porosity trends with depth seen in compilations by Mondol et al. (2007) are driven by lithology (Aplin et al., 1995; Yang & Aplin, 2004). Clay-rich sediments have higher porosities and higher compressibilities at deposition than coarser, or clay-poor, sediments leading to these drastically different compression curves. At high stresses though, compression curves are found to converge

(Casey et al., 2019) and form one common trend of porosity vs. depth for depths larger than 1000 m (Ewy et al., 2020). Similarly, the large variability in permeability at a given porosity, as can be seen in compilations by Neuzil (1994), is driven by lithology (Schneider et al., 2011; Yang & Aplin, 2007, 2010). The higher the clay content, the lower the vertical permeability at the same porosity. However, no systematic study has been published yet in which a natural marine mudstone has been admixed with silt in varying concentrations to quantify and model the influence of grain size on both the compression and permeability behavior.

Here, I present results on the impact of grain size on compressibility and permeability of mudstones from seaward of the Nankai deformation front, offshore Japan. I mixed marine mudstone with silt-size silica in varying concentrations, then resedimented these mixtures in the laboratory, and subjected them to one-dimensional compression to vertical effective stresses of 21 MPa. I show that compressibility systematically decreases and permeability systematically increases with decreasing clay-size fraction. I apply empirical compression and permeability models to predict petrophysical properties outside of measured ranges and for grain sizes not covered by the data set. The results will aid studies in more accurately predicting pore pressure and effective stress in the Nankai accretionary prism as well as other continental margins by providing better controls on the initial sediment properties and their hydromechanical relationships. Additionally, the results will provide material properties of mudstones which are important to understand earthquake generation in accretionary prisms (e.g., Dixon & Moore, 2007; Kitajima & Saffer, 2012; Schumann et al., 2014) and microbial behavior in the deep subseafloor (e.g., Heuer et al., 2020).

2 Geologic Background

The Nankai accretionary prism is located southeast of Japan and is formed by the northwestward subduction of the Philippine Sea Plate beneath the Eurasian Plate at ~ 4-6 cm yr^{-1} (Miyazaki & Heki, 2001) (Figure 1). This subduction created the Shikoku Basin during the early to middle Miocene (Kobayashi et al., 1995; Okino et al., 1994). Sedimentary deposits within the Shikoku Basin and the overlying Quaternary trench wedge are actively accreting at the deformation front (Tobin et al., 2009).

The Shikoku Basin has been a target for several Ocean Drilling Program (ODP) and Integrated Ocean Drilling Program (IODP) investigations. Many of them are part of the Nankai

Trough Seismogenic Zone Experiment (NanTroSEIZE) project. During IODP Expedition 322, the incoming sedimentary strata and uppermost igneous basement of the Shikoku Basin, offshore Kii Peninsula, were sampled and logged (Underwood et al., 2010a). This expedition was aimed at understanding the initial pre-subduction conditions because the down-dip evolution of the initial properties of the sediment is what ultimately changes slip behavior along the plate interface from aseismic to seismic (Hyndman et al., 1997; Moore & Saffer, 2001; Vrolijk, 1990). Two sites were drilled during Expedition 322 along the Kumano transect: Site C0011 on the northwestern flank of the bathymetric high called Kashinosaki Knoll and Site C0012 near the crest of the seamount (Figure 1). I present results from Site C0011. Drilling at Site C0011 occurred in 4048.7 m water depth and cored a 536 m thick succession of the incoming sediment section in Hole B (the uppermost 340 meters were not cored), while measurement-while-drilling (MWD) and logging-while-drilling (LWD) data had been collected in Hole A during the previous IODP Expedition 319.

At Site C0011, four lithostratigraphic units are present in the incoming sediment section (from base to top) (Figure 2): (1) a ~26 m thick middle Miocene (~14.0 Ma) volcaniclastic-rich facies, (2) a ~176 m thick middle Miocene (~14.0 to ~12.2 Ma) Lower Shikoku Basin (LSB) turbidite facies, (3) a ~195 m thick middle to late Miocene (~12.2 to ~9.1 Ma) Lower Shikoku Basin (LSB) hemipelagic facies, and (4) a ~139 m thick late Miocene (~9.1 to ~7.6 Ma) Middle Shikoku Basin (MSB) facies. As coring did not start until 340 mbsf (Saito et al., 2010), the Upper Shikoku Basin (USB) facies was not sampled at Site C0011 during IODP Expedition 322. However, it was subsequently sampled in Hole C and D during IODP Expedition 333.

The volcaniclastic-rich facies is dominated by tuffaceous silty claystone and light gray tuff with minor occurrences of tuffaceous sandy siltstone (Underwood et al., 2010b). The LSB turbidite facies is composed of bioturbated silty claystone with abundant interbeds of dark gray clayey siltstone (deposited by muddy turbidity currents) and fine-grained siliciclastic sandstone (deposited by sandy turbidity currents) (Underwood et al., 2010b). The LSB hemipelagic facies is dominated by heavily bioturbated silty claystone, typical of the hemipelagic deposits in the Shikoku Basin (Underwood et al., 2010b). The lower part of the MSB facies is composed of bioturbated silty claystone, volcaniclastic sandstone, and dark grey siltstone, whereas the upper part consists of moderately lithified bioturbated silty claystone with interbeds of tuffaceous

196 sandstone (Underwood et al., 2010b). This facies also includes a chaotic interval representative
197 of a mass transport deposit (Underwood et al., 2010b).

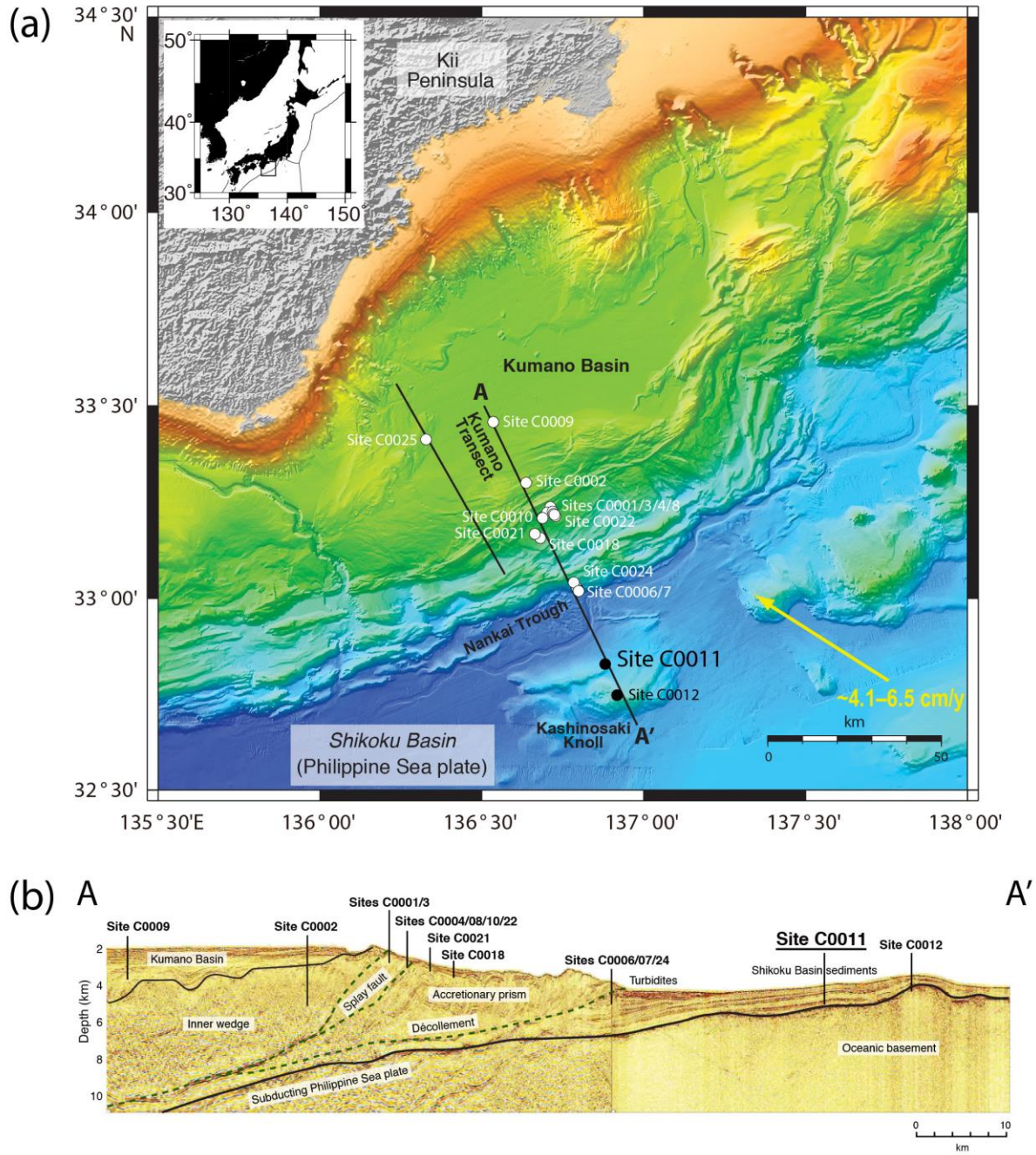

198

199 **Figure 1**. (a) Bathymetric map of the Shikoku Basin (modified from Tobin et al. (2020)) and (b) seismic cross
200 section of the IODP NanTroSEIZE drilling transect from the Kumano Basin to the Kashinosaki Knoll (modified
201 from Underwood et al. (2010b)). Solid dots = Expedition 322 sites, open dots = previous NanTroSEIZE sites. Site
202 C0011 is ~15 km seaward of the deformation front. The yellow arrow indicates the convergence between Philippine
203 Sea plate and Japanese Islands (Eurasian plate). Black line labeled A – A' in Figure 1a shows the location of the

seismic profile in Figure 1b. Black lines in Figure 1b encompass the accretionary complex and green dashed lines indicate major megasplay faults.

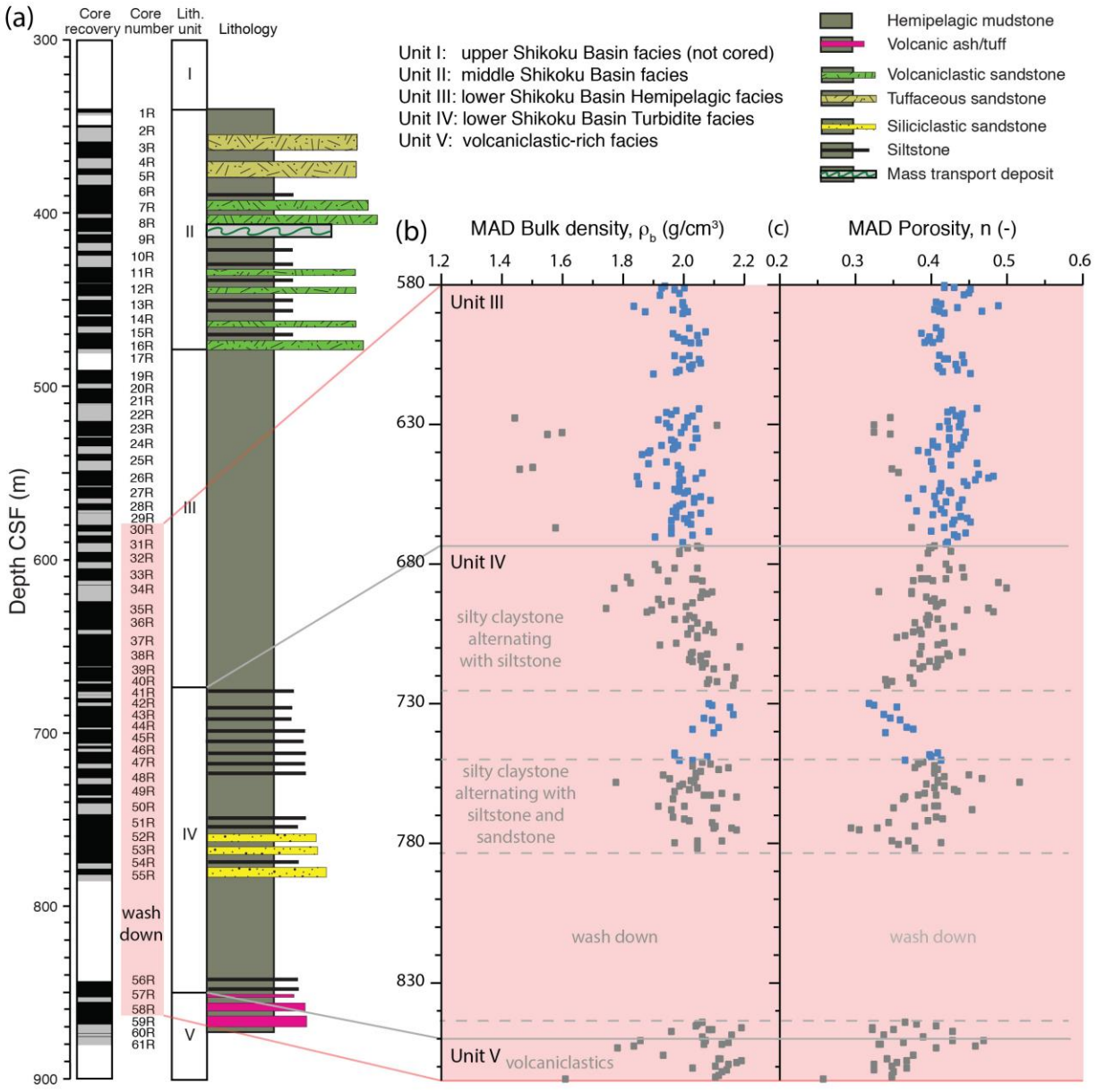

Figure 2. (a) Stratigraphic section from continuous sampling and core descriptions in Hole C0011B with core recovery **(**after Underwood et al., 2010b**)**. Red box extending from cores 30R to 58R indicates depth range over which sediment samples were collected, ground, combined, and homogenized to a bulk powder of Nankai mudstone. CSF stands for core depth below seafloor. (b) Moisture and density (MAD) bulk density and (c) porosity for the depth range sampled here. Blue data points are the ones used for regression in Figure 7; grey data points are omitted in the regression in Figure 7 because of erroneous measurements or the presence of siltstones, sandstones, and volcaniclastics, or lack of core due to wash down.

3 Samples and Experimental Methods

3.1 Samples

About 25 kg of marine mudstones were collected from Hole C0011B during IODP Expedition 322. The majority originated from the LSB turbidite and hemipelagic facies, while up to 15% of the sediments came from the top section of the volcaniclastic-rich facies. Specifically, the sediments are from cores 30R to 58R, corresponding to depths between 580.4 mbsf and 865.72 mbsf (red box, Figure 2). Assuming hydrostatic conditions, the in situ effective stress for the midpoint depth of 680.75 mbsf is interpreted to be 5.5 MPa, which is consistent with calculated hydrostatic vertical effective stresses on intact samples. Hüpers and Kopf (2012) and Guo and Underwood (2014) reported hydrostatic vertical effective stresses ranging between 4.58 and 5.73 MPa. However, the samples' maximum past effective stresses (preconsolidation stresses) ranged from 5.6 to 11.7 MPa, indicating overconsolidation. Samples were preferentially taken from mud-prone, homogeneous, sections and air-dried on large trays at room temperature. When the mass remained constant, the material was ground in small batches in a ball grinder, sieved, and then homogenized to a bulk powder. For the remainder of this paper, I refer to this material as Nankai mudstone. For sediment mixtures, I added silt-size silica (MIN U SIL 40), crystalline quartz purchased from US Silica, to the Nankai mudstone in the following proportions of mudstone to silica: 100:00, 88:12, 76:24, 64:36, 52:48, and 40:60. Details on how sediment samples were prepared are described in the section "Resedimentation".

Grain size measurements were performed on the sediment mixtures composed of Nankai mudstone and silica in the ratios of 100:00, 88:12, 76:24, 64:36, 52:48, and 40:60 using the hydrometer technique in accordance to ASTM D7928 guidelines (ASTM International, 2017). Resulting grain size distributions show that these mixtures are comprised of 56%, 50%, 48%, 41%, 36%, and 32% clay-size particles by mass, respectively (Table 1). For details on the particle size measurements of all sediment mixtures refer to Reece et al. (2013). The grain density (ρ_g) of the Nankai mudstone averages to 2680 kg/m^3 based on moisture and density (MAD) measurements made onboard the *JOIDES Resolution*, and is reported by the vendor as 2650 kg/m^3 for the silica. Grain densities of the remaining sediment mixtures were determined by weighting both constituents proportionally. Clay fractions by mass (cf_m) can then be converted into clay fractions by volume (cf_v) (Table 1):

$$cf_v = 1 - \frac{\rho_g}{\rho_{Qz}} \cdot (1 - cf_m) \quad \text{(Eq. 1)}$$

The mineralogic composition of the Nankai mudstone was measured by Macaulay Scientific Consulting LTD in Aberdeen, UK and is provided in Reece et al. (2013). Both whole rock and <2μm clay-size fraction analyses were performed by X-ray powder diffraction (XRPD). The bulk sample contains (in order of abundance): clay minerals, quartz, plagioclase, K-feldspar, and minor amounts of calcite, pyrite, and halite. The clay-size fraction (< 2μm) is dominated by smectite with lesser amounts of illite, chlorite and kaolinite, indicating an origin well above the smectite – illite transition. The mineralogies of both the bulk sample and clay size-fraction are in overall agreement with shipboard XRPD measurements of bulk powders (Saito et al., 2010) and clay mineral assemblages published by Underwood and Guo (2013), respectively.

Atterberg Limits, specifically the liquid limit (w_L), plastic limit (w_P), and plasticity index (I_P), were measured (Table 1) following the procedure in ASTM D4318 (ASTM International, 2018). The liquid and plastic limits were determined using the Multipoint Method and Hand Rolling Method, respectively. For details on the Atterberg Limits of the sediment mixtures and a plasticity chart refer to Reece et al. (2013).

Table 1. *Mass and Volumetric Clay Fractions and Atterberg Limits of Nankai Sediment Mixtures.*

Nankai mudstone [%]	**Silt [%]**	**ρ_g [g/cc]**	**cf_m**	**cf_v**	**w_L [%]**	**w_P [%]**	**I_P [%]**
100	0	2.680	0.560	0.555	60	29	31
88	12	2.676	0.500	0.495	54	26	28
76	24	2.673	0.480	0.476	51	22	29
64	36	2.669	0.410	0.406	45	20	25
52	48	2.666	0.360	0.356	40	20	20
40	60	2.662	0.320	0.317	35	19	16

Note. Original source is Reece et al. (2013). ρ_g = grain density; for Nankai mudstone, grain density values from moisture and density (MAD) data were averaged over the depth range that the Nankai mudstone originated from; for other mixtures, a grain density of 2650 kg/m^3 was used for the silica (as reported by the vendor) and weighted averages were calculated. cf_m = mass clay fraction. cf_v = volumetric clay fraction (see Equation 1). w_L = liquid limit. w_P = plastic limit. I_P = plasticity index.

3.2 Resedimentation

Resedimentation is an incremental, uniaxial consolidation method that follows the procedure of a conventional oedometer test to compress a slurry of sediment. Because Site C0011 is located seaward of the deformation front, where deposition is largely uniaxial, resedimentation is a valid technique to understand geomechanical behavior of ocean sediments on the incoming sea plate. Resedimentation simulates the process of natural sedimentation and burial in the laboratory under controlled and repeatable conditions and was first developed in the civil engineering community (Sheahan, 1991; Santagata & Kang, 2007) but has since been successfully employed in the field of geology (Adams et al., 2013; Casey et al., 2013, 2019; Day-Stirrat et al., 2011; Reece et al., 2013; Schneider et al., 2011). Unlike intact samples recovered from core sections that often show signs of disturbance and may significantly vary in composition and grain size from one centimeter to the next, resedimented samples are homogeneous and do not suffer from potential biases imposed by disturbance or remolding during coring and recovery. Additionally, the fact that it is very repeatable makes it an ideal technique for systematic experiments studying fundamental behavior, like the impact of grain size on hydromechanical behavior of marine mudstones.

Sediment slurries were prepared by mixing 500 g dry mass of sediment mixture with de-ionized water and 26 g/L sodium chloride (sea salt). This salt concentration, when combined with the residual salinity contained in the dry sediment, resulted in a pore fluid salinity equal to that of seawater. The 500 g dry mass consisted of Nankai mudstone and silt-size silica in the following mass ratios: 100:00, 88:12, 76:24, 64:36, 52:48, and 40:60. Using a water content of 105% for the Nankai mudstone ensured a stable slurry with no gravimetric settling. The addition of silica required an additional 33% of water per silica fraction. The slurries were well mixed and de-aired under a vacuum and poured into consolidometers. Then I incrementally loaded the slurries for several weeks up to a maximum total stress of 100 kPa following the general procedures of an oedometer test in ASTM D2435/D2435M (ASTM International, 2020) while

allowing the sediments to freely drain pore fluids at both ends of the specimen. The samples were then unloaded to an overconsolidation ratio of four (OCR = 4, σ_v = 25 kPa) prior to being extruded from the consolidometers.

3.3 Uniaxial Consolidation

Constant rate of strain (CRS) consolidation experiments provide a means to understand consolidation behavior of the sediment mixtures to higher stresses, simulating burial under partially drained conditions. The resedimented samples were trimmed into a confinement ring for uniaxial CRS testing to continuously measure porosity, compressibility, and permeability as a function of vertical effective stress. Using a Trautwein GeoTAC Sigma-1 CRS load frame in accordance with ASTM Standard D4186/D4186M (ASTM International, 2012), sediment mixtures were subjected at a constant axial strain rate to vertical effective stresses of 21 MPa. Axial strain rate was adjusted to stay within a pore pressure ratio of 3-15% following ASTM Standard D4186/D4186M (ASTM International, 2012). For details on the CRS experiments refer to Reece et al. (2013).

4 Results

4.1 Experimental Data on Sediment Mixtures

4.1.1 Compression Behavior

Compression curves of the Nankai mudstone – silt mixtures are shown in Figure 3 and comprise the resedimentation data (large symbols) and CRS data (small symbols). The individual data sets were previously published by Reece et al. (2013). Void ratios decrease with increasing vertical effective stress for all sediment mixtures and partially recover during unloading (Figure 3, unloading not shown for resedimentation), as is typical for consolidation of soils and sediments (e.g., Holtz & Kovacs, 1981). Good agreement is generally observed between the compression results obtained from both methods (resedimentation and CRS tests). The compression behavior of the sediment mixtures follows the behavior commonly observed in the geotechnical community. The decline in void ratio (e = n/(1-n), where n is porosity) during burial is commonly assumed to be proportional to the log of vertical effective stress (σ'_v):

$$e = e_0 - C_c \log_{10}\left(\frac{\sigma'_v}{\sigma'_0}\right), \quad \text{(Eq. 2)}$$

where e_0 and σ'_0 are parameters that are empirically derived in zones where the vertical effective stress and void ratio are known. Here, e_0 is the void ratio at a reference vertical effective stress σ'_0 of 1 kPa for resedimentation experiments and 1 MPa for CRS experiments. The compression index (C_c) is the slope of the log-linear relationship between void ratio and stress. However, the measured virgin compression lines are curved surfaces. This means the compression curves cannot be accurately described by a single C_c. Instead, C_c decreases with increasing stress level, particularly for clay-rich samples. Therefore, I define C_c over varying stress ranges: 2.6 – 100 kPa (resedimentation) as well as 0.2 – 1 MPa, 1 – 5 MPa, and 5 – 20 MPa (CRS) (Table 2). Except for the two end-members (56% and 32% clay), all sediment mixtures display a consecutive decrease in C_c by a factor ranging between 1.8 and 1.4 across all stress levels (Table 2, Figure 3). The expansion index (C_e) is the slope of the log-linear relationship between void ratio and effective stress during unloading. All samples were unloaded during CRS testing to an overconsolidation ratio (OCR) of 4 (σ'_v ~ 5.2 MPa). Therefore, C_e is determined over the stress range of 21 – 5 MPa and varies between 0.07 for the most clay-rich sample and 0.04 for the least clay-rich sample (Table 2, Figure 3).

Table 2. *Consolidation Results from Resedimentation and Constant Rate of Strain (CRS) Consolidation Tests of Nankai Mudstone – Silt Mixtures.*

			Resedimentation		Measured CRS						Fitted ln(v) vs. ln(σ'_v)			
Nankai mudstone [%]	Silt [%]	cf_v	e_0 at 1 kPa	C_c[a] [MPa^{-1}]	P'_c [MPa]	e_0 at 1 MPa	C_c[b] [MPa^{-1}]	C_c[c] [MPa^{-1}]	C_c[d] [MPa^{-1}]	C_c [MPa^{-1}]	ln(1+e_0)	v_0	C	R^2
100	0	0.56	2.77	-0.62	0.117	0.96	0.66	0.48	0.36	-0.07	0.671	1.968	-0.116	0.9972
88	12	0.50	2.63	-0.60	0.091	0.86	0.56	0.43	0.32	-0.06	0.620	1.869	-0.108	0.9981
76	24	0.48	2.44	-0.57	0.115	0.79	0.50	0.39	0.31	-0.06	0.581	1.797	-0.102	0.9989
64	36	0.41	2.11	-0.47	0.109	0.69	0.43	0.34	0.29	-0.04	0.525	1.699	-0.094	0.9991
52	48	0.36	1.80	-0.38	0.108	0.68	0.34	0.29	0.27	-0.03	0.518	1.681	-0.082	0.9997
40	60	0.32	1.72	-0.37	0.100	0.67	0.25	0.24	0.24	-0.04	0.514	1.669	-0.069	0.9981

Note. Silt = silt-size silica (US MIN U SIL 40 purchased from US Silica). cf_v = volumetric clay fraction rounded to two digits after the decimal point. CRS = constant rate of strain consolidation test. e_0 = reference void ratio at 1 kPa (resedimentation) or 1 MPa (CRS). C_c = compression index (2.6-100 kPa = derived from resedimentation tests; 0.2-1 MPa, 1-5 MPa, and 5-20 MPa = derived from CRS tests). C_e = expansion index. v_0 = (1+e_0) = specific volume at a vertical effective stress of unity (1 MPa). C = compression index in log-log space of specific volume and effective stress. R^2 = coefficient of determination.

The compression behavior significantly changes with clay fraction. The initial void ratio (e_i), which is the first void ratio digitally measured during resedimentation at 2.6 kPa,

346 systematically decreases from 2.51 to 1.57 for clay fractions decreasing from 56% to 32% clay
347 (Table 2, Figure 3). A similar trend exists for the first void ratio values during CRS testing,
348 which decrease from 1.63 to 0.97. The compression index (C_c) at the beginning of CRS testing
349 (0.2 – 1 MPa) decreases by a factor of 2.6 from 0.66 to 0.25 (Table 2) indicating that the
350 sediment mixtures become stiffer the less clay they contain (Figure 3). However, this difference
351 becomes less dominant with increasing stress level. At high stress levels (5 – 20 MPa), C_c only
352 decreases by a factor of 1.44 from 0.36 to 0.25 (Table 2). This observation, along with the
353 reducing initial void ratio for decreasing clay fractions, results in a cross-over in compression
354 curves (Figure 3).

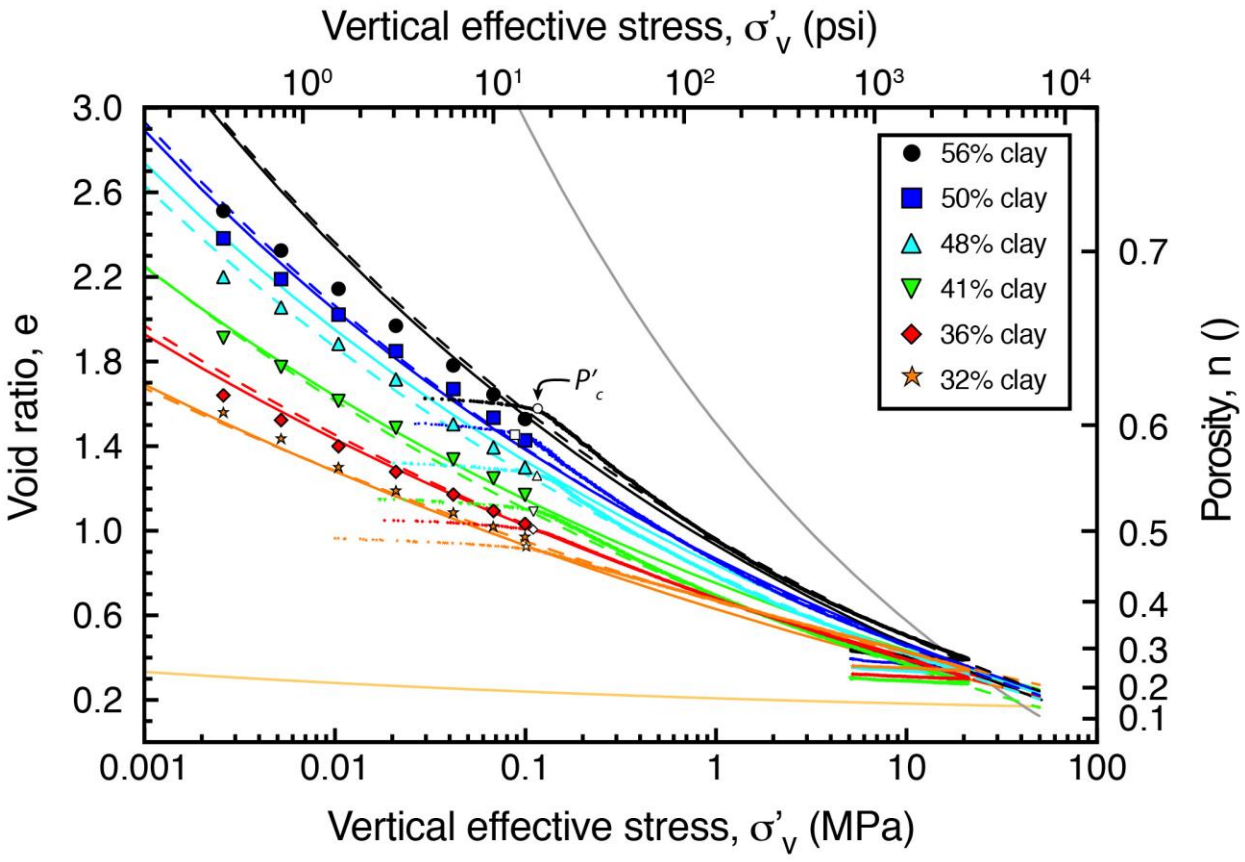

355

356 **Figure 3**. Compression behavior of the six Nankai mudstone – silt mixtures. Smaller symbols represent constant
357 rate of strain (CRS) consolidation test data, while larger symbols represent resedimentation data. Preconsolidation
358 stresses (P_c'), indicated by small open symbols, are derived using the work-stress method **(**Becker et al., 1987**)**.
359 Regressions were fit to both resedimentation and CRS data sets for each sediment mixture using the Butterfield
360 **(**1979**)** method (dashed lines). Measured compression and fitting parameters are listed in Table 2. Thin solid lines
361 represent the predictions of compression curves for the clay fractions corresponding to the six sediment mixtures

using the model presented herein. Predicted compression curves for pure clay (gray) and pure silt (yellow) are included.

Electron microscopy illuminates the pore-scale effects on the microstructure resulting from consolidation (Figure 4). The most clay-rich sample (56% clay) has small pores within the clay matrix (Figure 4a), while the most silt-rich sample (32% clay) has very large pores (~7 μm) that are concentrated around silt grains, as well as zones of smaller pores more characteristic of the clay-rich sample (Figure 4b). While it may seem as if the silt-rich sample has a much larger porosity than the clay-rich sample at the maximum vertical effective stress of 21 MPa, in reality, their porosities are almost identical (Figure 3). As the very compressible and porous clay particles get replaced by added solid silt-size quartz grains, the porosity and compressibility of the bulk mixtures are being reduced. This results in the above mentioned cross-over in compression curves and the fact that all compression curves seem to merge at large stresses.

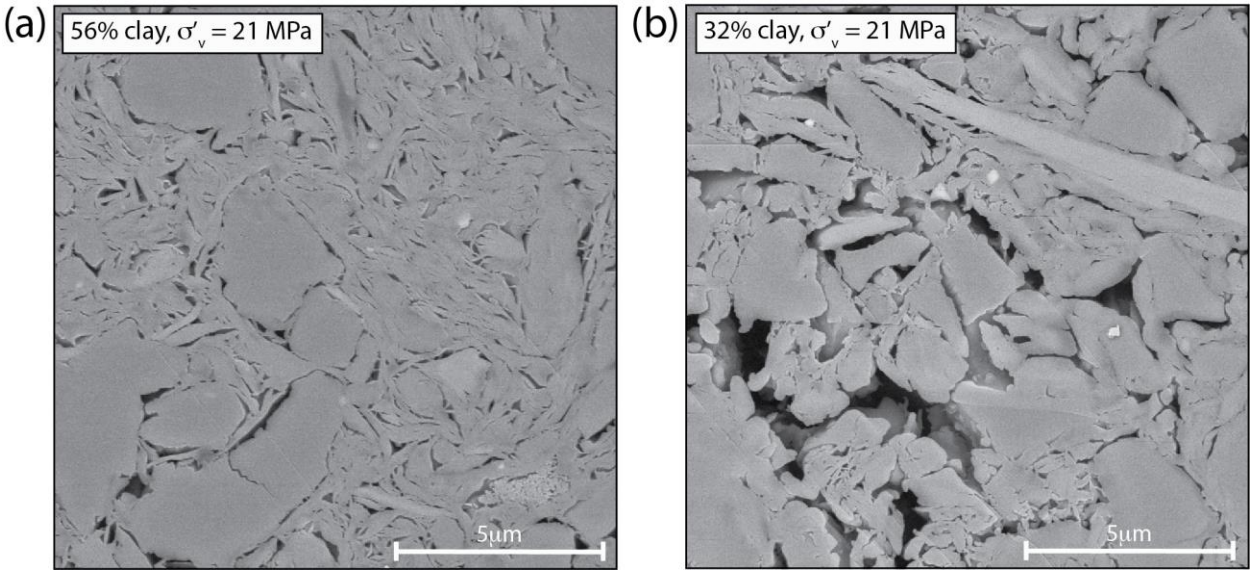

Figure 4. Microstructure of Nankai mudstone – silt mixtures (modified from Reece et al., 2013). (a) Backscattered electron (BSE) image of the pure Nankai mudstone with 56% clay-size particles after compression to 21 MPa. (b) BSE image of Nankai mudstone admixed with silt resulting in 32% clay-size particles, also compressed to 21 MPa. Images represent vertical cross-sections of samples (i.e., load was applied from the top of the images).

The preconsolidation stress (P_c') is the maximum vertical effective stress a sample has experienced in the past. It is characterized by an inflection point in the compression curve, which separates the elastic behavior represented by the flat reloading part of the compression curve, where deformation is reversible, from the elasto-plastic behavior represented by the steep virgin compression curve, where deformation is largely irreversible. For the Nankai mudstone – silt

mixtures investigated here, this is the stress that the sediment mixtures were preloaded to during resedimentation. Preconsolidation stresses of all mixtures are derived from the CRS test data using the work-stress method (Becker et al., 1987) and range between 91 kPa and 117 kPa (Table 2), confirming the past maximum vertical stress of ~100 kPa in the resedimentation tests.

A power-law relationship between specific volume ($v = 1 + e$) and vertical effective stress, as developed by Butterfield (1979), best models the concave up compression curves over the entire stress range (Figure 3):

$$v = v_0(\sigma'_v)^C, \quad \text{(Eq. 3)}$$

where v_0 is the specific volume at a reference vertical effective stress (σ'_v) of 1 MPa and C is an empirical constant. I used a log-log plot of specific volume vs. vertical effective stress and constrained v_0 and C through linear regression: for the Nankai mudstone, I find C = -0.116 and v_0 = 1.968 at 1 MPa when units of MPa are used, while parameters for the remaining mixtures are listed in Table 2. This power-law model fits void ratios across the entire stress range (Figure 3, dashed lines), including resedimentation and CRS data, and models void ratios that are consistent with measured values. For the most clay-rich sample (56% clay), however, noticeably lower void ratios were measured during resedimentation compared to the power-law model. This could be a result of increased sidewall friction, which underestimates the vertical effective stress.

4.1.2 Permeability Behavior

The permeability – porosity relationships of the Nankai mudstone – silt mixtures are shown in Figure 5 and comprise the resedimentation data (large symbols) and CRS data (small symbols). Only the permeability and porosity data from CRS testing were previously published by Reece et al. (2013). The permeability behavior of the sediment mixtures follows the behavior commonly observed for mudstones and other lithologies, where vertical permeability declines logarithmically with decreasing porosity for all sediment mixtures (Figure 5). This log-linear relationship between vertical permeability (k) and porosity (n) can be described as:

$$log_{10}(k) = \gamma\, n + log_{10}(k_0)\,, \quad \text{(Eq. 4)}$$

where γ is the slope of the log-linear relationship and k_0 is the y-intercept at a porosity of zero. Across all stress levels and sediment mixtures, porosities range between 0.7 and 0.25 and vertical permeabilities range between 10^{-15} and 10^{-20} m^2 (Figure 5). Good agreement is generally

observed between the permeability results obtained from both methods (resedimentation and CRS tests). For the most clay-rich sample (56% clay), however, vertical permeabilities are noticeably higher in resedimentation tests than modeled by the log-linear relationship fit to both data sets. This could possibly be a result of increased sidewall friction for this particular experiment, as mentioned above for the compression results, or it could be attributed to Terzaghi's one-dimensional consolidation theory overestimating the true permeability of the mudstone (Mesri and Olson, 1971; Taylor, 1942), or simply an error in the calculated porosity of the sample during resedimentation.

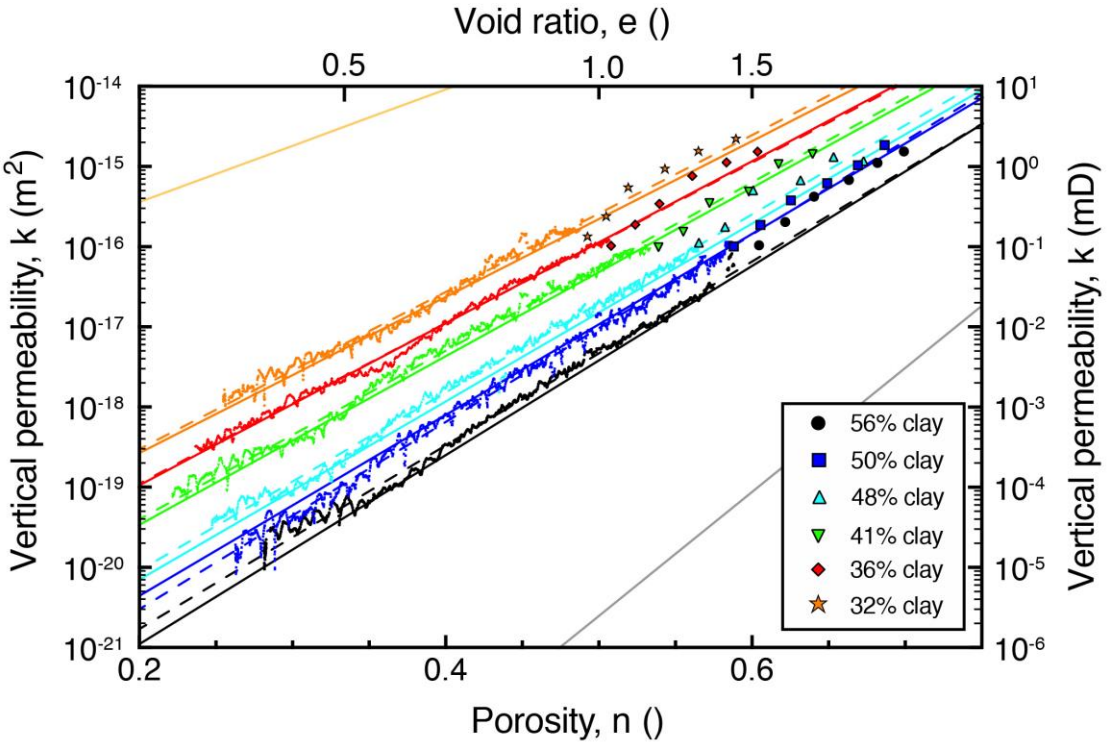

Figure 5. Vertical permeability behavior of the six Nankai mudstone – silt mixtures. Smaller symbols represent constant rate of strain (CRS) consolidation test data (shown are 15-point moving averages), while larger symbols represent resedimentation data. Linear regressions were fit to both resedimentation and CRS data sets for each sediment mixture (dashed lines). Regression parameters are listed in Table 3. Thin solid lines represent permeability – porosity predictions for the clay fractions corresponding to the six sediment mixtures using the geometric mean model presented herein following Schneider et al.'s (2011) approach. Predicted permeability – porosity relationships for pure clay (gray) and pure silt (yellow) are included.

The permeability behavior significantly changes as a function of clay fraction. Vertical permeability of the most clay-rich mixture (56% clay) is lowest at all stresses (porosities) and consecutively increases with decreasing clay fraction at a given porosity (Figure 5). The rate at

which vertical permeability declines with reducing porosity varies with clay fraction. Permeability of the most clay-rich sample decreases by five orders of magnitude over porosities ranging from 0.7 to 0.3, while permeability of the most silt-rich sample decreases by only three orders of magnitude over porosities ranging from 0.6 to 0.25. This results in a divergence of the permeability-porosity relationships with increasing stress or decreasing porosity (Figure 5) and is consistent with the decrease in γ from 11.42 to 9.68 and increase in $\log(k_0)$ from -23.04 to -20.44 with decreasing clay fraction (Table 3).

Table 3. *Permeability Results from Resedimentation and Constant Rate of Strain (CRS) Consolidation Tests of Nankai Mudstone – Silt Mixtures.*

Nankai mudstone [%]	**Silt [%]**	cf_v	γ	**log(k_0) [m^2]**	R^2	**k_i [m^2]**
100	0	0.56	11.42	-23.04	0.994	4.50×10^{-19}
88	12	0.50	11.72	-22.88	0.992	8.65×10^{-19}
76	24	0.48	11.06	-22.25	0.995	1.98×10^{-18}
64	36	0.41	10.44	-21.47	0.993	6.62×10^{-18}
52	48	0.36	9.99	-20.95	0.995	1.43×10^{-17}
40	60	0.32	9.68	-20.44	0.986	3.46×10^{-17}

Note. Silt = silt-size silica (US MIN U SIL 40 purchased from US Silica). cf_v = volumetric clay fraction rounded to two digits after the decimal point. γ = slope of the fitted (log)permeability – porosity relationship. $\log(k_0)$ = intercept of the fitted (log)permeability – porosity relationship at porosity of 0. R^2 = coefficient of determination for permeability-porosity fits. k_i = in situ permeability determined by projecting (log)permeability – porosity relationship to average porosity of 0.41.

Scanning electron backscatter images provide insights into pore-scale effects on the permeability resulting from consolidation (Figure 4). The increase in vertical permeability with decreasing clay fraction is due to the preservation of large pores by a process called silt-bridging, as previously described by (Schneider et al., 2011). The increasing amounts of quartz grains form stress bridges which carry most of the applied vertical load. As a result, larger and more connected pore spaces are kept open in between these silt grain clusters (Figure 4b) leading to increased permeabilities.

I model the permeability – porosity behavior of all sediment mixtures by fitting a linear relationship following Equation 4 through both the resedimentation and CRS test data (Figure 5, dashed lines). The model parameters that best fit the Nankai mudstone are $\log(k_0)$ = -23.04 and γ = 11.42 (Table 3). Model parameters for the remaining sediment mixtures are listed in Table 3. Especially for the clay-rich sample (56% clay), permeabilities measured during resedimentation

tend to be higher than the modeled permeabilities. This could be related to the increased sidewall friction mentioned above for this particular experiment.

4.2 Predictive Models

4.2.1 Butterfield Compression Model

Having six sediment samples composed of the exact same mineralogies but differing in the clay-size fractions allows for the development of a predictive compression model. Through this model void ratios can be predicted at any stress and for any clay fraction within this specific Nankai mudrock system. I plot the fitting parameters C and v_0, determined for each sediment mixture by applying Butterfield's (1979) method (Table 2), as a function of clay fraction (Figure 6). The compression model parameters C and v_0 linearly decrease and increase with volumetric clay fraction (cf_v), respectively (Figure 6). Linear regressions of the data provide the following relationships between the compression model parameters and volumetric clay fractions:

$$C = -0.1891\ cf_v - 0.0122 \quad \text{with } R^2 \text{ of } 0.9694 \qquad \text{(Eq. 5)}$$

$$v_0 = 1.2651\ cf_v + 1.226 \quad \text{with } R^2 \text{ of } 0.9152 \qquad \text{(Eq. 6)}$$

The application of this model to the volumetric clay fractions of the investigated Nankai sediment mixtures shows good agreement with the measured values (Figure 3, solid lines). The largest difference between predicted and modeled/measured void ratios can be observed for the mixture with 48% clay. This can be explained by the grain size distribution results. While even increments in silt were added to the Nankai mudstone, grain size results documented a non-proportional jump to larger clay fractions for this particular mixture. This compression model provides the mechanism to predict void ratios at varying stresses for any clay fraction within this mudrock system. For different types of mudstones though, the model parameters will vary depending on clay mineralogy, grain size distribution, and other textural properties. They can be determined if compression behavior is known from at least three independent samples with different clay fractions.

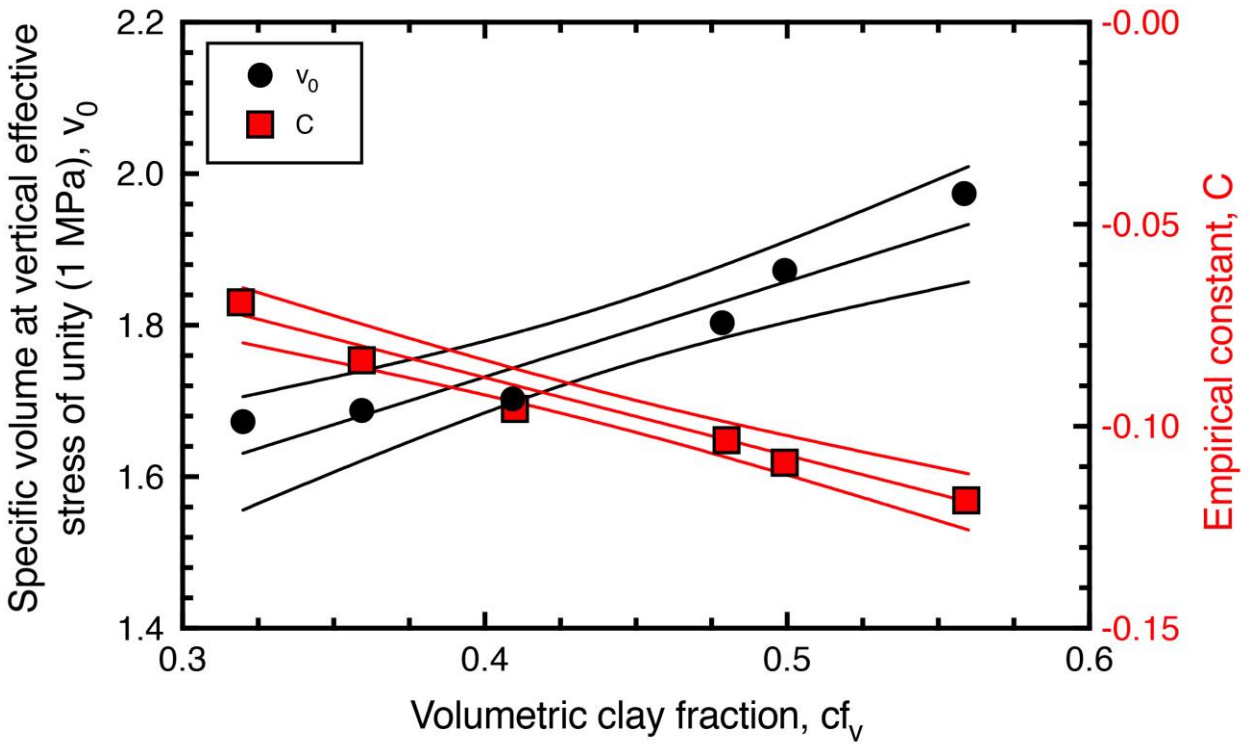

Figure 6. Compression model parameters for the six Nankai mudstone – silt mixtures as a function of volumetric clay fraction. Model parameters v_0 and C are derived using the modified Butterfield (1979) approach. Solid outer lines indicate the 95% confidence intervals.

4.2.2 Geometric Mean Permeability Model

The effective permeability of a mudstone can be approximated by the geometric mean of the permeabilities of the clay and silt component, following the method presented in Schneider et al. (2011):

$$k_{eff} = k_{cl}^{cf_v} \cdot k_{si}^{(1-cf_v)} \quad , \qquad \text{(Eq. 7)}$$

where k_{cl} is the permeability of the clay domain and k_{si} is the permeability of the silt domain. This model assumes that the mudstone is composed of randomly distributed clay domains with clay particles and small pores and silt domains with silt grains and large pores; therefore, both the clay and silt fractions have porosity and contribute to flow (Schneider et al., 2011). By combining Equations 4 and 7 and assuming that porosity in both domains is the same ($n = n_{cl} = n_{si}$), the effective permeability can be defined as:

$$log\left(k_{eff}\right) = \left[cf_v \cdot \gamma_{cl} + (1 - cf_v) \cdot \gamma_{si}\right] \cdot n + cf_v \cdot log\left(k_0^{cl}\right) + (1 - cf_v) \cdot log\left(k_0^{si}\right) \qquad \text{(Eq. 8)}$$

Equation 8 describes the effective permeability of any clay-silt mixture as a function of porosity by using the permeability behavior of the two end members and knowledge of volumetric clay fraction (c_{fv}). I solve for the four unknown parameters with multivariable linear regressions. The model parameters for this particular system of Nankai mudstone and silt-size silica are $\log(k_0^{cl}) = -28.37$, $\gamma_{cl} = 15.54$, $\log(k_0^{si}) = -16.83$, $\gamma_{si} = 7.02$. The geometric mean model provides a remarkably accurate prediction of the permeability variation in Nankai sediments with clay fraction (Figure 5, solid lines). Predicted permeabilities are extremely close to the regression lines of the six Nankai – silt mixtures.

5 Discussion

5.1 Parent Material: Nankai Mudstone (56% clay)

5.1.1 Compression Behavior

Laboratory compression curves of intact mudstone mostly lie above the compression curve of my resedimented Nankai mudstone and show higher compressibilities (e.g., compare squares, diamonds, and triangles with black dashed line, Figure 7). The compression curves of intact core samples from Site C0011 were previously measured in incremental loading tests (Hüpers & Kopf, 2012; Kitajima & Saffer, 2014) and constant rate of strain consolidation tests (Guo & Underwood, 2014; Kitajima & Saffer, 2014). Only intact core samples from the same depth range as the Nankai mudstone and from either hemipelagic or silty clay facies are chosen for this comparison. Two out of the seven intact core samples considered here (tests T70_197 and U_212 in Kitajima & Saffer, 2014) were recompressed in the laboratory to much larger stresses (65 and 85 MPa, respectively) than the others and have compressibilities that are very close to the one of the resedimented Nankai mudstone (compare triangles with black dashed line, Figure 7).

The field compression curve is described by the moisture and density (MAD) void ratio measurements of the intact core (blue lines, Figure 7); it lies above the compression curve of the resedimented Nankai mudstone (black dashed line, Figure 7). Thus, the field samples bear a higher vertical effective stress at a given void ratio than the resedimented Nankai mudstone (Figure 7). Although the field curve bears a higher vertical stress, the slope of the field curve is

much steeper (higher apparent compressibility) than any sample compressed in the laboratory (Figure 7).

The preconsolidation stress (P_c') is the maximum past stress the rock has experienced. It is often inferred from the stress-strain behavior during compression. For example, when a field sample is unloaded during sampling and then reloaded in the laboratory, its preconsolidation stress is imaged as the transition from more elastic behavior (flat portion of recompression curve) to more plastic behavior (steep portion of recompression curve) (orange lines, Figure 8). At this geographic location, there are no reported erosional events and it is interpreted that the present day effective stress is the maximum past effective stress (crosses, Figure 7). None the less, the observed preconsolidation stresses are greater than the in-situ effective stresses (circled crosses, Figure 7). The degree of overconsolidation is commonly quantified as the ratio of the current effective stress to the preconsolidation stress. At this location, the overconsolidation ratio ranges between 1 and 3 (Guo & Underwood, 2014; Hüpers & Kopf, 2012; Kitajima and Saffer, 2014) and, in fact, increases from 1.50 to 2.52 over 98 to 862 mbsf based on data by Kitajima and Saffer (2014) (Figure 7). Because the past effective stress is not interpreted to be greater than the present effective stress, the overconsolidation in this location is referred to as apparent.

Several processes could explain the difference between the field compression curve and the laboratory-based compression curves. For example, if overpressure was present, then the actual effective stresses would be lower than the field compression curve (e.g., Bekins et al., 1995; Davis et al., 1983; Ellis et al., 2015; Flemings & Saffer, 2018; Saffer & Bekins, 1998, 2006; Suppe, 2007; Wang, 1994). Rapid deposition of low permeability sediments can generate this pore fluid overpressure because the fluids cannot escape fast enough as the sediments compact (Gibson, 1958; Gordon & Flemings, 1998). However, an analytical solution for sedimentation above an impermeable base, following Gibson (1958), indicates no overpressure at Site C0011. The degree of overpressure is controlled by Gibson's time factor, $T_g = m^2\, t/c_v$, where m is the sedimentation rate, t is total time and c_v is hydraulic diffusivity. At Site C0011, the average sedimentation rate from the seafloor to the bottom of the Lower Shikoku Basin facies at 850 mbsf is 0.06 mm/yr and the total time span is 14 Mio. years (Saito et al., 2010). Based on the hydromechanical results presented in this study, hydraulic diffusivity (c_v) of the Nankai mudstone is 5x 10^{-8} m^2/s. Gibson's (1958) analytical solution produces a time factor (T_g)

of 0.03, corresponding to an overpressure ratio (λ^*) of ~0% supporting the assumption of hydrostatic pressures. Therefore, overpressure cannot explain the significant difference between field and laboratory behavior.

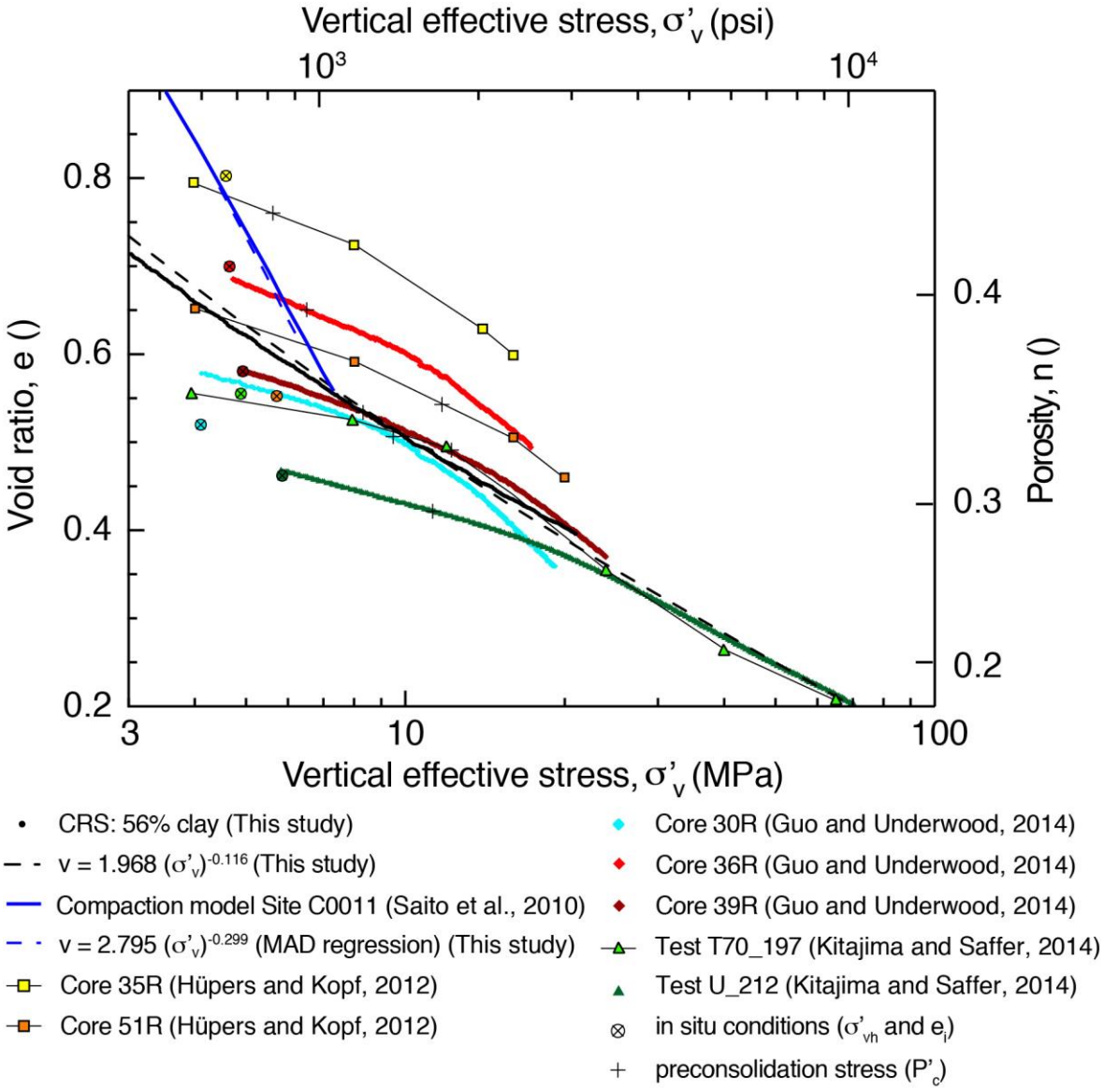

Figure 7. Comparison of compression behavior of resedimented Nankai mudstone with previously published results. I assume hydrostatic pressure conditions for the conversion from depth to vertical effective stress. Resedimented Nankai mudstone is shown as small black circles along with its compression model using Butterfield's (1979) method (black dashed line), where *v* is specific volume (= e + 1). Blue line is the field-based modeled porosity – effective stress behavior, based on MAD data and derived over the entire depth range at Site C0011 assuming hydrostatic fluid pressure. Blue dashed line is the modeled void ratio – effective stress behavior using Butterfield's (1979) method on MAD data that fall only in the sampled depth range and are from hemipelagic sediments (see blue symbols in Figure 2). Previously published compression curves of intact samples were derived

from incremental loading tests (squares and triangles) and constant rate of strain consolidation tests (diamonds and triangles) and are plotted starting roughly at their in situ hydrostatic vertical effective stresses and through the virgin compression curve. Their compression indices (C_c) are derived from the virgin compression lines over stresses between 12 and 24 MPa for all intact core samples except test U_212, for which the stress ranges between 29 and 85 MPa. The reload and unload portions of these tests are omitted for clarity. Only samples from the same depth range as the resedimented Nankai mudstone and from either hemipelagic or silty clay facies are shown.

A more likely explanation is secondary consolidation, also known as creep. Creep refers to time-dependent deformation (volumetric and shear) under constant effective stress conditions due to the displacement and readjustment of particle contacts and deformation of micropores in clay aggregates (Mitchell & Soga, 2005; Wood, 1990). In Figure 8, I have presented the compression curves as a logarithmic function of time: $e = e_1 - C_\alpha \ln \frac{t}{t_1}$, where e is void ratio, e_1 is the void ratio at the end of primary consolidation (following pore pressure dissipation), t is time, t_1 is a reference time, and C_α is the coefficient of secondary consolidation, also often termed secondary consolidation index. In fact, whether rocks of this age follow this simple rate behavior is not known (Karig and Ask, 2003). I infer that the Lower Shikoku Basin sediments have undergone creep in the following manner. At laboratory timescales, their compression behavior would follow line 't_1'. However, because deposition of the Lower Shikoku Basin sediments was extremely slow, there has been significant creep in addition to mechanical compression. Thus, for example, points B, C, and D, have undergone creep with the result that they have lower void ratios than they would have if they laid on the laboratory compression curve (compare blue symbols and blue line vs. thin solid black line in Figure 8). Interestingly, when these samples are reloaded (orange lines, Figure 8), they have a 'memory' and will deform elastically until they reach the laboratory compression curve, where upon they will compress along 't_1'. Thus, I infer that the apparent overconsolidation is recording creep and that the creep is greater with deeper and older samples. Karig and Ask (2003) observed a similar behavior and suggested that primary and secondary consolidation proceed simultaneously during burial and that strain over a given decade in time increases with time.

The resedimented compression curve is different than the compression curves of intact samples, however, they merge at high stresses (Figure 8). I attribute this difference to the development fabric in intact rocks that does not have time to develop in resedimented material. In a naturally deposited soft clay, the grains are held together by chemico-physical bonds

(Skempton & Jones, 1944; Terzaghi, 1941), where the particles and particle groups flocculate, resulting in an initially open fabric of edge-to-edge and edge-to-face contacts between elongate and platy particles and particle groups in a cardhouse arrangement (Mitchell & Soga, 2005). This fabric is often referred to as metastable fabric (point A/A' in Figure 8; Mitchell & Soga, 2005) and gives the in situ material strength. In contrast, in the laboratory, the process of resedimentation removes the in situ fabric that was created in the sediment during initial deposition and does not provide enough time for the fabric to re-develop due to loading rates that are hundred to thousand times more rapid than in nature. Therefore, the resedimented compression curve is shifted to the left of the virgin compression curve, meaning that in situ fabric can carry effective stresses during consolidation that are higher than its resedimented counterpart at the same void ratio (Figure 8). However, at higher stresses, the natural in situ fabric progressively collapses during burial. Thus, the structures of both intact and resedimented sediments become more similar, and the difference between their compression curves decreases till the in situ fabric is completely broken down at their point of convergence (Burland, 1990) (Figure 8).

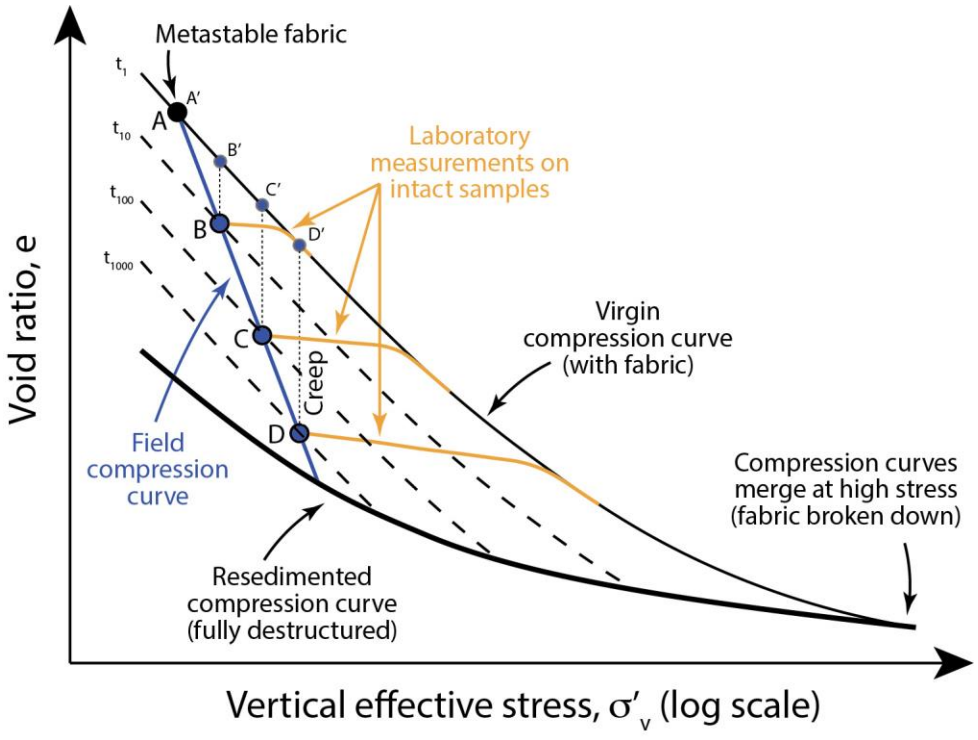

Figure 8. Schematic view of void ratio as a function of the logarithm of vertical effective stress, explaining the differences in compression curves observed in Figure 7. The field compression curve (blue line), consisting of void

ratio measurements (A - D) acquired as part of the moisture and density (MAD) dataset, is much steeper and has lower void ratios than the normal or virgin compression curve of intact core because of increasing creep with depth/stress. The dashed lines indicate amounts of creep, where each increment of creep (equal amount of strain or reduction in void ratio) is interpreted as an order of magnitude in time. More strain (or void ratio reduction) occurs at higher stresses (e.g., D' – D) than at lower stresses (B' – B), resulting in the increased apparent compressibility of the field compression curve. Intact whole round core samples that were recompressed in the laboratory (orange) by other researchers show apparent overconsolidation and fall on the virgin compression curve. The resedimented compression curve (bold black line) is stiffer and at lower void ratios because of the lack of a metastable fabric.

5.1.2 Permeability Behavior

The permeability vs. porosity behavior of the resedimented Nankai mudstone is strikingly similar to that observed in intact samples of mudstones from similar depths at Site C0011 (Figure 9). Except for one core sample (test U_212 in Kitajima & Saffer, 2014), all in situ permeabilities determined from incremental loading, constant rate of strain consolidation, or flow-through experiments on intact samples fall approximately within ± half a log cycle of the permeabilities of the resedimented Nankai mudstone (Figure 9). In fact, three measurements lie on top of the measured permeability – porosity trend of the resedimented Nankai mudstone (core 43R in Dugan & Zhao (2013); core 36R in Guo & Underwood (2014); core 51R in Hüpers & Kopf (2012)). The estimated in situ permeability of the Nankai mudstone is determined by projecting its permeability-porosity relationship (dashed line in Figure 9) to the average porosity of 0.41 (MAD porosity averaged over the sampled depth interval) and is equal to 4.54×10^{-19} m^2. This measurement is almost identical to the in situ permeability measured on core 36R (Guo & Underwood, 2014). So, while the compression behavior of the resedimented Nankai mudstone does not match that observed in intact samples, the permeability vs. porosity behavior does. Therefore, the impact of remolding sediments during the resedimentation process is less significant on the permeability than the compression behavior.

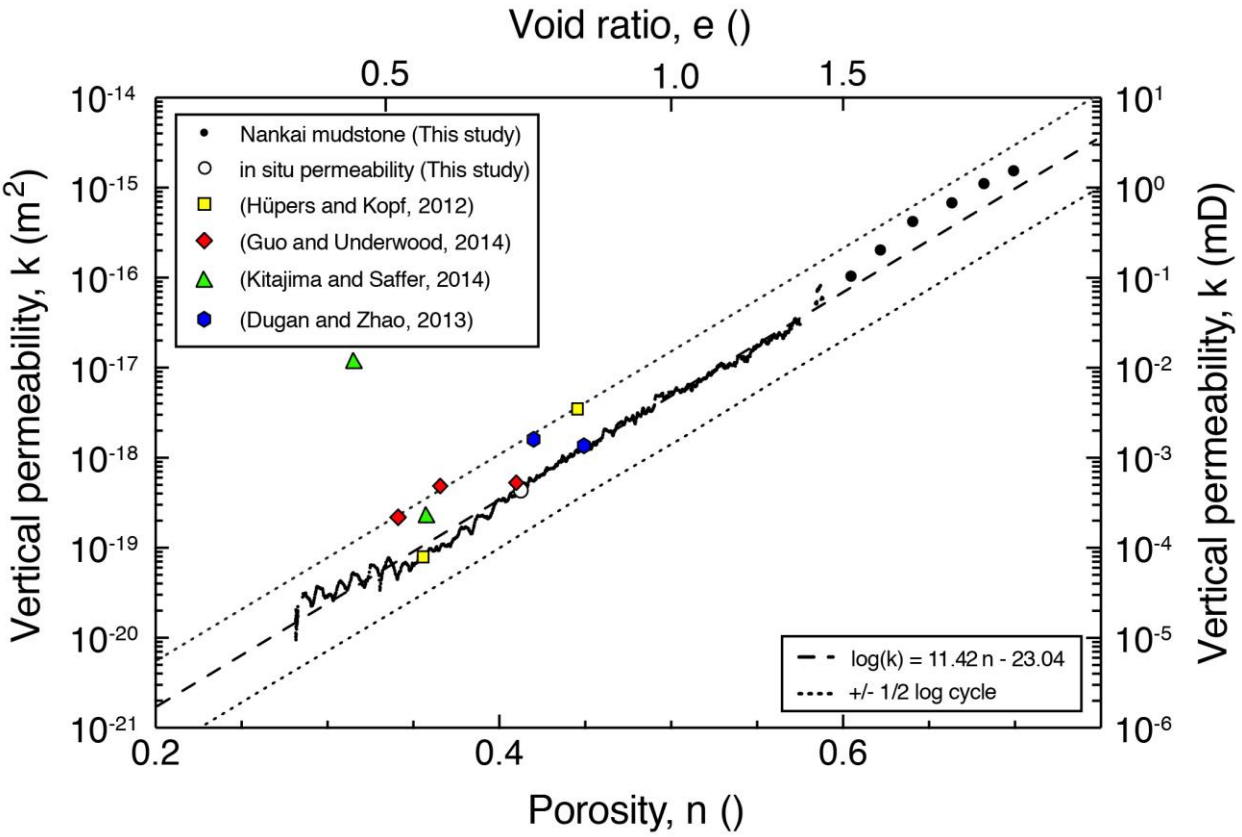

Figure 9. Comparison of vertical permeability of resedimented Nankai mudstone with previously published results. Resedimented Nankai mudstone is shown as large black circles (resedimentation) and small black circles (CRS) along with its permeability model (dashed line). Hollow round symbol represents in situ permeability projected to average in situ porosity of 0.41 using this permeability model (dashed line). Yellow squares are in situ permeabilities derived from incremental loading tests, red diamonds are in situ permeabilities derived from constant rate of strain consolidation tests, green triangles are in situ permeabilities derived from both incremental loading and constant rate of strain consolidation tests, and blue hexagons are in situ permeabilities measured in flow-through experiments. The in situ permeabilities all fall approximately within ± half a log cycle (dotted lines) of the resedimented Nankai mudstone permeability. Only samples from the same depth range as the Nankai mudstone and from either hemipelagic or silty clay facies are shown.

5.2 Sediment Mixtures

Compression indices (C_c) of all sediment mixtures, constrained between vertical effective stresses of 5 and 20 MPa, vary between 0.36 and 0.25 and systematically decline with decreasing clay content (Table 2, Figure 10a). At low stresses, these C_c values are significantly lower than those of intact samples (see C_c values constrained over 12 -24 MPa in Figure 10a); at high stresses though, they are similar (see C_c values constrained over 24 - 65 MPa and 29 - 85 MPa in Figure 10a). I already discussed that the virgin compression curves for the intact samples are

steeper (i.e., higher C_c) than the resedimented compression curve at low stresses but merge with one another at high stresses due to the combined effects of creep and fabric differences. This explanation reflects the observed differences in compression indices.

The inferred in situ permeability (k_i) is the permeability at the in situ porosity. I determine k_i values of the sediment mixtures by projecting the individual permeability-porosity relationships with their respective k_0 and γ values (Table 3) to the average in situ porosity of 0.41. In situ permeabilities of resedimented mixtures vary between 4.5 x 10^{-19} and 3.46 x 10^{-17} m^2 and systematically decline with decreasing clay fraction (Table 3, Figure 10b). When comparing in situ permeabilities on a depth profile, k_i of the Nankai mudstone is quite similar to those of most intact core samples (Figure 10b), confirming the observations made based on Figure 9. Not surprisingly, the sediment mixtures have increasingly higher k_i values with decreasing clay content (Figure 10b). In contrast to the compression behavior, the permeability behavior appears to be less affected by the remolding process.

The coefficient of consolidation (c_v), also referred to as hydraulic diffusivity, is calculated from the compression and permeability behavior. I determined c_v values for all sediment mixtures by converting compression index (C_c) into coefficient of volume compressibility (m_v) and applying the following relationship between in situ permeability (k_i) and m_v with a fluid viscosity (μ_w) of 0.001002 Pa s for a temperature of 20°C: $c_v = \frac{k_i}{(m_v\, \mu_w)}$ (see Supporting Information). The c_v value for the Nankai mudstone (1.05 x 10^{-8} m^2/s) is quite similar to those I calculated for intact core samples based on the C_c and k_i values from Figures 10a and b. However, not surprisingly, the sediment mixtures have increasingly higher c_v values with decreasing clay fraction, copying the trend observed in the in situ permeability behavior.

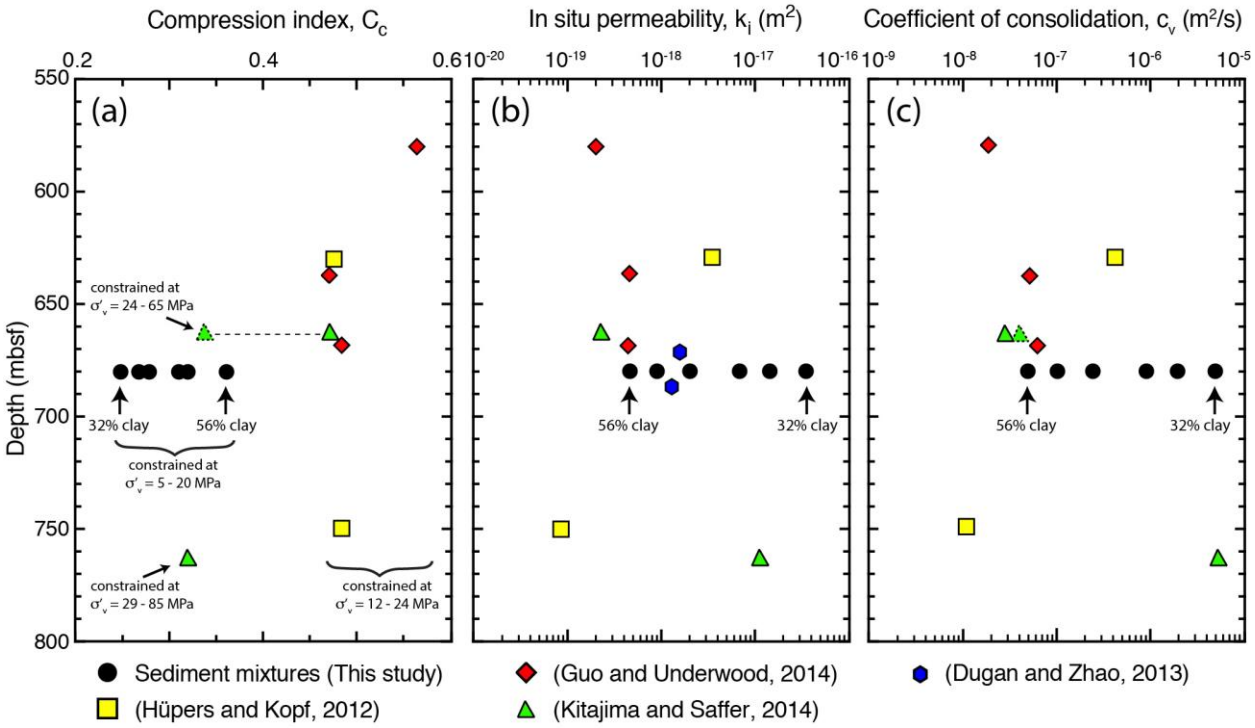

Figure 10. Comparison of (a) compression indices, (b) in situ permeabilities, and (c) coefficient of consolidation of the six Nankai mudstone – silt mixtures with previously published results. Depth range shown is limited to the source depth for the Nankai mudstone (i.e., cores 30R to 58R) and only samples from this depth range and from either hemipelagic or silty clay facies are included. Nankai mudstone - silt mixtures are plotted at the same midpoint depth of 681 mbsf and shown as black circles. Yellow squares are reported C_c and k_i derived from incremental loading tests, red diamonds are C_c values I calculated based on the authors' compression data and reported k_i derived from constant rate of strain consolidation tests, green triangles are C_c values I calculated based on the authors' compression data and reported k_i derived from both incremental loading and constant rate of strain consolidation tests, and blue hexagons are reported k_i measured in flow-through experiments. C_v is calculated from C_c and k_i ($c_v = k_i/(m_v\ \mu_w)$) by converting C_c to coefficient of volume compressibility (m_v) and using a fluid viscosity (μ_w) of 0.001002 Pa s (see Supporting Information).

5.3 Model Evaluation

In my compression model, the parameters C and v_0 vary as a function of volumetric clay fraction. The model successfully predicts compression behavior for all six Nankai mudstone – silt mixtures (Figure 3, solid lines). Specifically, it captures well the declining C_c with increasing stress level validating the use of the Butterfield (1979) model rather than a log-linear relationship between effective stress and void ratio or an exponential relationship between effective stress and porosity. The observation that C_c continuously decreases from early compression (σ'_v = 0.2 – 1 MPa) to late compression (σ'_v = 5 – 20 MPa) has been previously observed for other marine

703 mudstones (Casey et al., 2019; Kitajima & Saffer, 2014; Long et al., 2011;). Especially
704 sediments with high liquid limits and smectite contents demonstrate a strong non-linear behavior
705 in C_c with increasing stress as described by Casey et al. (2019), who studied 15 different
706 resedimented mudstones.

707 While coefficients of determination for Equations 5 and 6 are above 0.9, the limitation in
708 the compression model is the reduced accuracy towards end-member compositions. Because the
709 predictive compression model is only constrained over volumetric clay fractions (cf_v) ranging
710 from 0.56 to 0.32, the extrapolation of C and v_0 to cf_v values outside of this range introduces
711 higher potential errors as can be seen by the increasing range in the 95% confidence levels
712 (Figure 6). That said, the estimated v_0 values at end-member cf_v of 0 and 1 provide reasonable
713 values: v_0 = 1.226 (equivalent to e_0 = 0.226 or n_0 = 0.18) at cf_v = 0 and v_0 = 2.4911 (equivalent to
714 e_0 = 1.4911 or n_0 = 0.60) at cf_v = 1. Porosities of 0.18 for the pure silt and 0.60 for the pure clay
715 are within range of possible values. The porosity in an ideal rhombohedral packing of equally
716 sized spheres is 0.26. In this study though, the silt-size grains are not all equally sized and perfect
717 spheres. Therefore, a lower number than 0.26 is expected. The porosity of a pure clay is more
718 dependent on the clay mineral type, shape, and size, and thus, is more variable. Ultimately, the
719 relationship between v_0 and cf_v reflects the fabric and packing structure. Estimated C values at
720 end-member cf_v of 0 and 1 also provide reasonable values: C = -0.0122 at cf_v = 0 and C = -0.2013
721 at cf_v = 1. Because C is the power to which the vertical effective stress is raised in its relationship
722 with specific volume (Equation 3), a higher absolute value of C, as observed for the pure clay,
723 means an increased curvature, i.e. the rate at which specific volume decreases with increasing
724 stress level slows down with consolidation. For low clay contents, however, the rate at which
725 specific volume decreases with increasing stress level is nearly constant. This can be captured by
726 a C value of almost zero for the pure silt (cf_v = 0). Ultimately, the relationship between C and cf_v
727 reflects the compressibility of the sample.

728 The geometric mean permeability model successfully predicts permeabilities for all six
729 Nankai mudstone – silt mixtures (Figure 5, solid lines). The model parameters, derived using the
730 geometric mean model and multivariable linear regression, are specific to this mudrock system
731 and will vary for different types of mudstones. Schneider et al. (2011) used this technique and
732 applied it to sediment mixtures composed of Boston Blue Clay and the same silt-size silica,
733 allowing for a direct comparison. The model parameters predicted here for the pure silt (log (k_0^{si})

= -16.83, γ_{si} = 7.02) are very similar to the ones predicted by Schneider et al. (2011) (log (k_0^{si}) = -17.23, γ_{si} = 6.43). This should come as no surprise; it is rather a validation in the approach, as both studies use the exact same silt-size silica. However, the model parameters for the pure clay in the Nankai mudstone (log (k_0^{cl}) = -28.37, γ_{cl} = 15.54) indicate a much more drastic permeability decline with porosity than observed for the pure clay in the Boston Blue Clay (log (k_0^{cl}) = -22.61, γ_{cl} = 8.15) (Schneider et al., 2011). This significant difference is a result of varying clay mineralogy, grain size distribution, and grain angularity (Schneider et al., 2011). The Nankai mudstone used in this study is very similar to the Boston Blue Clay used in Schneider et al. (2011) in terms of grain size (56 wt% vs. 57 wt%). But the bulk mineralogy is drastically different. The Nankai mudstone contains 24 wt% quartz, 16 wt% feldspar, and 59 wt% clay minerals, of which smectite is the majority (Reece et al., 2013), while the Boston Blue Clay is an illitic glaciomarine clay (Kenney, 1964) and is composed of illite + illite – smectite, muscovite, and trioctahedral mica with lesser amounts of chlorite, hydrobiotite, and kaolinite (Schneider et al., 2011). This illustrates how mineralogy alone can have a huge impact on the hydrological properties of marine mudstones.

5.4 Implications for Subduction Zone Systems

I document porosity, permeability, and compressibility of mudstones on the incoming sea plate at the Nankai Trough as a function of stress and provide models to predict hydromechanical properties of sediments as a function of grain size. Characterizing the in situ compression and permeability properties of subduction inputs is critical in order to relate input sediments to those at frontal thrust regions and understand the mechanics of accretionary prisms, plate boundary earthquakes, fault and slow slip, and microbial behavior in the subsurface of subduction zones. Here, I have provided a model to describe the systematic change in permeability as a function of porosity and lithology. This is a key input that will inform models of subduction zone hydrogeology and microbial activity. Other models developed to understand earthquakes, fault slip, or slow slip rely on the understanding of material behavior, and in particular both permeability and hydraulic diffusivity, which I have provided insight for. My observations imply that with small changes in stress as sediment enters the accretionary prism, significant fluid loss may occur due to compression (analogous to sensitive soils) as the sediment cannot hold those stresses and will lose porosity. This would create a significant fluid, and hence a pressure source

764 in the accretionary prism. The results presented here do not only apply to the Nankai Trough but
765 also any other collisional continental margin.

766 **6 Conclusions**

767 I used six sediment mixtures composed of varying proportions of hemipelagic mudstone
768 from the incoming sea plate at the Nankai Trough and silt-size silica to document the impact of
769 grain size on porosity (void ratio), permeability, and compressibility as a function of stress. Key
770 results are:

771 • Compression behavior of clay-silt mixtures can be effectively described by a power-law
772 relationship between specific volume and vertical effective stress.

773 • Over the entire stress range, void ratio and compression index decrease systematically
774 with decreasing clay fraction.

775 • At higher stresses, void ratios and compression indices of all mixtures tend to converge
776 above ~10 MPa into a much narrower range.

777 • The difference between compression curves of field samples, intact cores recompressed
778 in the laboratory, and resedimented samples is due to a combination of increasing creep
779 with depth and a difference in fabric.

780 • The compression behavior of mudstones is more affected by the remolding process
781 during resedimentation than the permeability behavior.

782 • Permeability behavior of clay-silt mixtures can be effectively described by a log-linear
783 relationship between permeability and porosity.

784 • Vertical permeability of the most clay-rich sample is around two orders of magnitudes
785 lower than that of the most silt-rich sample.

786 • Vertical permeability of the most clay-rich sample decreases five orders of magnitude
787 over porosities ranging from 0.7 to 0.3, while permeability of the most silt-rich sample
788 decreases by only three orders of magnitude over porosities ranging from 0.6 to 0.25.

- With decreasing clay fraction, the amount of small, elongated, and crescent-shaped pores in the matrix declines and large, jagged pore throats between silt grains are preserved resulting in a dual-porosity system.
- Applied compression and permeability models using Butterfield's (1979) approach and a geometric mean, respectively, accurately predict hydromechanical behavior of clay-silt mixtures.

Acknowledgments, Samples, and Data

This research used samples and data provided by the International Ocean Discovery Program (IODP). Funding for this research was provided by U.S. Science Support Program for IODP through the Schlanger Ocean Drilling Fellowship awarded to J.R. In addition, the U.T. Geofluids Consortium supported this project. Datasets for this research are included in this paper (and its supplementary information files): Reece et al. (2013). The moisture and density porosity data can be obtained from the IODP CDEX SIO7 data center (http://sio7.jamstec.go.jp). All other data supporting the discussion and conclusions can be obtained from the tables within this paper.

References

Adams, A. L., Germaine, J. T., Flemings, P. B., & Day-Stirrat, R. J. (2013), Stress induced permeability anisotropy of Resedimented Boston Blue Clay, *Water Resources Research*, *49*, 1-11, doi:10.1002/wrcr.20470.

Aplin, A. C., Yang, Y. L., & Hansen, S. (1995), Assessment of beta, the compression coefficient of mudstones and its relationship with detailed lithology, *Marine and Petroleum Geology*, *12*(8), 955-963, doi:10.1016/0264-8172(95)98858-3.

ASTM International (2020), Standard Test Methods for One-Dimensional Consolidation Properties of Soils Using Incremental Loading (D2435/D2435M), in Soil and Rock (I), edited by *Annual Book of ASTM Standards*, 04.08, 14 pp, American Society for Testing and Materials, West Conshohocken, PA, doi:10.1520/D2435-20.

ASTM International (2018), Standard Test Methods for Liquid Limit, Plastic Limit, and Plasticity Index of Soils (Standard D4318), in Soil and Rock (I), edited by *Annual Book of ASTM Standards*, 04.08, 20 pp, American Society for Testing and Materials, West Conshohocken, PA, doi:10.1520/D4318-18.

ASTM International (2012), Standard Test Method for One-Dimensional Consolidation Properties of Saturated Cohesive Soils Using Controlled-Strain Loading (Standard D4186/D4186M), in Soil and Rock (I), edited by *Annual Book of ASTM Standards*, 04.08, 18 pp, American Society for Testing and Materials, West Conshohocken, PA, doi:10.1520/D4186-12.

ASTM International (2017), Standard Test Method for Particle-Size Distribution (Gradation) of Fine-Grained Soils Using the Sedimentation (Hydrometer) Analysis (D7928), in Soil and Rock (I), edited by *Annual Book of ASTM Standards*, 04.08, 25 pp, American Society for Testing and Materials, West Conshohocken, PA, doi:10.1520/D7928-17.

Athy, L. F. (1930), Density, porosity, and compaction of sedimentary rocks, *Am. Assoc. Pet. Geol. Bull.*, *14*, 1-22.

Audet, P., Bostock, M. G., Christensen, N. I., & Peacock, S. M. (2009), Seismic evidence for overpressured subducted oceanic crust and megathrust fault sealing, *Nature*, *457*, 76-78.

Baldwin, B., & Butler, C. O. (1985), Compaction curves, *Am. Assoc. Pet. Geol. Bull.*, *69*, 622-626.

Barker, D. H. N., Sutherland, R., Henrys, S., & Bannister, S. (2009), Geometry of the Hikurangi subduction thrust and upper plate, North Island, New Zealand, *Geochem. Geophys. Geosyst.*, 10:Q02007.

Becker, D. E., Crooks, J. H. A., Been, K., & Jefferies, M. G. (1987), Work as a criterion for determining in situ and yield stresses in clays, *Can. Geotech. J.*, *24*, 549-564.

Bekins, B. A., Dreiss, S., & McCaffrey, A. M. (1995), Episodic and constant flow models for the origin of low-chloride waters in a modern accretionary complex, *Water Resources Research*, *31*(12), 3205-3215, doi:10.1029/95WR02569.

Bennett, R. H., Bryant, W. R., & Hulbert, M. H. (1991), *Microstructure of fine grained sediments; from mud to shale*, 582 pp., Springer, New York - Berlin - Heidelberg - London - Paris - Tokyo - Hong Kong - Barcelona, United States.

Bethke, C. M. (1989), Modeling subsurface flow in sedimentary basins, *Geol. Rundsch.*, *78*(1), 129-154.

Bickle, M., Chadwick, A., Huppert, H. E., Hallworth, M., & Lyle, S. (2007), Modelling carbon dioxide accumulation at Sleipner: implications for underground carbon storage, *Earth Planet. Sci. Lett.*, *255*, 164–176.

Broichhausen, H., Littke, R., & Hantschel, T. (2005), Mudstone compaction and its influence on overpressure generation, elucidated by a 3D case study in the North Sea, *International Journal of Earth Sciences*, *94*(5-6), 956-978, doi:10.1007/s00531-005-0014-1.

Burland, J. B. (1990), On the compressibility and shear strength of natural clays, *Geotéchnique*, *40*(3), 329-378.

Butterfield, R. (1979), A natural compression law for soils (an advance on e-logp'), *Geotéchnique*, *29*, 469-480.

Carman, P. C. (1937), Fluid flow through granular beds, *Trans. Inst. Chem. Eng.*, *15*, 150-166.

Casey, B., Germaine, J. T., Flemings, P. B., Reece, J. S., Gao, B., & Betts, W. (2013), Liquid limit as a predictor of mudrock permeability, *Marine and Petroleum Geology*, *44*, 256-263, doi:10.1016/j.marpetgeo.2013.04.008.

Casey, B., Reece, J. S., & Germaine, J. T. (2019), One-dimensional normal compression laws for resedimented mudrocks, *Marine and Petroleum Geology*, *103*, 397-403, doi:10.1016/j.marpetgeo.2019.02.023.

Collins, K., & McGown, A. (1974), The form and function of microfabric features in a variety of natural soils, *Geotéchnique*, *24*(2), 223-254, doi:10.1680/geot.1974.24.2.223.

Daigle, H., & Dugan, B. (2009), Extending NMR data for permeability estimation in fine-grained sediments, *Marine and Petroleum Geology*, *26*(8), 1419-1427, doi:10.1016/j.marpetgeo.2009.02.008.

Davis, D., Suppe, J., & Dahlen, F. A. (1983), Mechanics of fold-and-thrust belts and accretionary wedges, *J. Geophys. Res.*, *88*, 1153-1173.

Day-Stirrat, R. J., Schleicher, A. M., Schneider, J., Flemings, P. B., Germaine, J. T., & van der Pluijm, B. A. (2011), Preferred orientation of phyllosilicates; effects of composition and stress on resedimented mudstone microfabrics, *Journal of Structural Geology*, *33*(9), 1347-1358, doi:10.1016/j.jsg.2011.06.007.

Dewhurst, D. N., Aplin, A. C., Sarda, J. P., & Yang, Y. L. (1998), Compaction-driven evolution of porosity and permeability in natural mudstones: An experimental study, *Journal of Geophysical Research*, *103*(B1), 651-661, doi:10.1019/97JB02540.

Dixon, T. H., & Moore, C., 2007, *The seismogenic zone of subduction thrust faults*, New York Chichester, West Sussex, Columbia University Press.

Dugan, B., & Flemings, P. B. (2000), Overpressure and fluid flow in the New Jersey continental slope: implications for slope failure and cold seeps, *Science*, *289*(5477), 288-291, doi:10.1126/science.289.5477.288.

Dugan, B., & Zhao, X. (2013), Data report: permeability of sediments from Sites C0011 and C0012, NanTroSEIZE Stage 2: Subduction inputs, in *Proc. IODP*, *322*, edited by S. Saito, M. B. Underwood, Y. Kubo and t. E. Scientists, Tokyo (Integrated Ocean Drilling Program Management International, Inc.), doi:10.2204/iodp.proc.322.208.2013.

Ellis, S., Fagereng, A., Barker, D., Henrys, S., Saffer, D., Wallace, L., et al. (2015), Fluid budgets along the northern Hikurangi subduction margin, New Zealand: The effect of a subducting seamount on fluid pressure, *Geophysical Journal International*, *202*(1), 277-297, doi:10.1093/gji/ggv127.

England, W. A., Mackenzie, A. S., Mann, D. M., & Quigley, T. M. (1987), The movement and entrapment of petroleum fluids in the subsurface, *Journal of the Geological Society London*, *144*, 327-347.

Ewy, R., Dirkswager, J., & Bovberg, C. (2020), Claystone porosity and mechanical behavior vs. geologic burial stress, *Marine and Petroleum Geology*, *121*, 104563, doi:10.1016/j.marpetgeo.2020.104563.

Expedition 326 Scientists (2011), NanTroSEIZE Stage 3: plate boundary deep riser: top hole engineering. *IODP Prel. Rept., 326*, doi:10.2204/iodp.pr.326.2011.

Flemings, P. B., Long, H., Dugan, B., Germaine, J. T., John, C., Behrmann, J. H., Sawyer, D. E., & IODP Expedition Scientists (2008), Pore pressure penetrometers document high overpressure near the seafloor where multiple submarine landslides have occurred on the continental slope, offshore Louisiana, Gulf of Mexico, *Earth and Planetary Science Letters*, *269*, 309-325, doi:10.1016/j.epsl.2007.12.005.

Flemings, P. B., & Saffer, D. M. (2018), Pressure and stress prediction in the Nankai accretionary prism: A critical state soil mechanics porosity-based approach, *J. Geophs. Res: Solid Earth*, *123*, 1089-1115, doi:10.1002/2017JB015025.

Gamage, K., & Screaton, E. (2006), Characterization of excess pore pressures at the toe of the Nankai accretionary complex, Ocean Drilling Program sites 1173, 1174, and 808: Results of one-dimensional modeling, *Journal of Geophysical Research*, *111*(B04103), doi:10.1029/2004JB003572.

Gamage, K., Screaton, E., Bekins, B., & Aiello, I. (2011), Permeability-porosity relationships of subduction zone sediments, *Marine Geology*, *279*(1-4), 19-36, doi:10.1016/j.margeo.2010.10.010.

Gibson, R. E. (1958), The progress of consolidation in a clay layer increasing in thickness with time, *Geotéchnique*, *8*, 171-182.

Gordon, D. S., & Flemings, P. B. (1998), Generation of overpressure and compaction-driven fluid flow in a Plio-Pleistocene growth-faulted basin, Eugene Island 330, offshore Louisiana, *Basin Res., 10*, 177-196.

Graue, K. (2000), Mud volcanoes in deepwater Nigeria, *Mar. Petrol. Geol., 17*, 959–974.

Green, D. H., & Wang, H. F. (1986), Fluid pressure response to undrained compression in saturated sedimentary rock, *Geophysics*, *51*, 948-956.

Guo, J., & Underwood, M. B. (2014), Data report: consolidation and permeability of sediments from Sites C0011, C0012, and C0018, IODP Expeditions 322 and 333, NanTroSEIZE Stage 2, In Saito, S., Underwood, M.B., Kubo, Y. and the Expedition 322 Scientists, *Proc. IODP*, *322*: Tokyo (Integrated Ocean Drilling Program Management International, Inc.), doi:10.2204/iodp.proc.322.209.2014.

Henry, P., Kanamatsu, T., Moe, K., & the Expedition 333 Scientists (2012), *Proceedings of the Integrated Ocean Drilling Program*, *333*: Tokyo (Integrated Ocean Drilling Program Management International, Inc.), doi:10.2204/iodp.proc.333.2012.

Heuer, V.B., Inagaki, F., Morono, Y., Kubo, Y., Spivack, A.J., Viehweger, B., Treude, T., Beulig, F., Schubotz, F., Tonai, S., Bowden, S.A., Cramm, M., Henkel, S., Hirose, T., Homola, K., Hoshino, T., Ijiri, A., Imachi, H., Kamiya, N., Kaneko, M., Lagostina, L., Manners, H., McClelland, H.-L., Metcalfe, K., Okutsu, N., Pan, D., Raudsepp, M.J., Sauvage, J., Tsang, M.-Y., Wang, D.T., Whitaker, E., Yamamoto, Y., Yang, K., Maeda, L., Adhikari, R.R., Glombitza, C., Hamada, Y., Kallmeyer, J., Wendt, J., Wörmer, L., Yamada, Y., Kinoshita, M., & Hinrichs, K.-U. (2020), Temperature limits to deep subseafloor life in the Nankai Trough subduction zone, *Science*, *370*, 1230-1234, doi:10.1126/science.abd7934.

Holloway, S. (2001), Storage of fossil fuel-derived carbon dioxide beneath the surface of the earth, *Ann. Rev. Energ. Env.*, *26*, 145–166.

Hubbert, M. K., & Rubey, W. W. (1959), Role of fluid pressure in mechanics of overthrust faulting, *Geol. Soc. Am. Bull.*, *70*, 115-166.

Hüpers, A., & Kopf, A. J. (2012), Data report: consolidation properties of silty claystones and sandstones sampled seaward of the Nankai Trough subduction zone, IODP Sites C0011 and C0012, in *Proc. IODP*, *322*, edited by S. Saito, M. B. Underwood, Y. Kubo and E. Scientists, p. 23, College Station, TX.

Huysmans, M., & Dassargues, A. (2006), Hydrogeological modeling of radionuclide transport in low permeability media: a comparison between Boom Clay and Ypresian Clay, *Environ. Geol.*, *50*(1), 122–131.

Hyndman, R. D., Yamano, M., & Oleskevich, D. A. (1997), The seismogenic zone of subduction thrust faults, *Island. Arc*, *6*, 244-260.

Karig, D. E. (1996), Uniaxial reconsolidation tests on porous sediments: Mudstones from Site 897, in *Proc. ODP, Sci. Results*, edited by R.B. Whitmarsh, D.S. Sawyer, A. Klaus, and D.G. Masson, *149*, College Station, TX.

Karig, D. E., & Ask, M. V. S. (2003), Geological perspectives on consolidation of clay-rich marine sediments, *J. Geophs. Res.*, *108*(B4), 2197, doi:10.1029/2001JB000652.

Kenney, T.C. (1964), Sea-level movements and the geologic histories of the post-glacial marine soils at Boston, Nicolet, Ottawa and Oslo, *Geotéchnique*, *14*, 203-230, doi:10.1680/geot.1964.14.3.203.

Kitajima, H., & Saffer, D. M. (2012), Elevated pore pressure and anomalously low stress in regions of low frequency earthquakes along the Nankai Trough subduction megathrust, *Geophys. Res. Lett.*, *39*(23), doi:10.1029/2012GL053793.

963 Kitajima, H., & Saffer, D. M. (2014), Consolidation state of incoming sediments to the Nankai
964 Trough subduction zone; implications for sediment deformation and properties,
965 *Geochemistry, Geophysics, Geosystems*, *15*(7), 2821-2839, doi:10.1002/2014GC005360.

966 Kobayashi, K., Kasuga, S., & Okino, K. (1995), *Shikoku Basin and its margins, in Backarc*
967 *Basins: Tectonics and Magmatism*, edited by B. Taylor, pp. 381-405, Plenum, New York.

968 Kozeny, J. (1927), Über kapillare Leitung der Wasser in Böden, *Royal Academy of Science*,
969 Vienna, Proc. Class, 136, 271-306.

970 Lallemand, S., Schnürle, P., & Malavieille, J. (1994), Coulomb theory applied to accretionary
971 and nonaccretionary wedges: possible causes for tectonic erosion and/or frontal accretion,
972 *J. Geophs. Res.*, *99*(B6), 12033-12055.

973 Lambe, T. W., & Whitman, R. V. (1969), *Soil Mechanics*, John Wiley and Sons, New York.

974 Liu, Y., & Rice, J. R. (2007), Spontaneous and triggered aseismic deformation transients in a
975 subduction fault model, *J. Geophys. Res.*, *112*, B09404.

976 Long, H., Flemings, P. B., Germaine, J. T., & Saffer, D. M. (2011), Consolidation and
977 overpressure near the seafloor in the Ursa Basin, deepwater Gulf of Mexico, *Earth and*
978 *Planetary Science Letters*, *305*(1-2), 11-20, doi:10.1016/j.epsl.2011.02.007.

979 Marty, B., Dewonck, S., & France-Lanord, C. (2003), Geochemical evidence for efficient aquifer
980 isolation over geological timeframes, *Nature*, *425*, 55–58.

981 Mesri, G., & Godlewski, P. M. (1977), Time- and stress-compressibility interrelationship,
982 *Journal of the Geotechnical Engineering Division*, *103*(GT5), 417-430.

983 Mesri, G., & Olson, R.E. (1971), Mechanisms controlling the permeability of clays, *Clays and*
984 *Clay Minerals*, *19*, 151-158.

985 Mikada, H., Becker, K., Moore, J. C., Klaus, A., et al. (2002), *Proc. ODP, Init. Repts.*, *196*,
986 College Station, TX (Ocean Drilling Program), doi:10.2973/odp.proc.ir.196.2002.

987 Milkov, A. V. (2000), Worldwide distribution of submarine mud volcanoes and associated gas
988 hydrates, *Mar. Geol.*, *167*, 29–42.

989 Mitchell, J. K., & Soga, K. (2005), *Fundamentals of soil behavior*, John Wiley and Sons, Inc., 3rd
990 ed., 558 p.

991 Miyazaki, S., & Heki, K. (2001), Crustal velocity field of southwest Japan: subduction and arc-
992 arc collision, *Journal of Geophysical Research*, *106*(B3), 4305-4326,
993 doi:10.1029/2000JB900312.

994 Mondol, N. H., Bjorlykke, K., Jahren, J., & Hoeg, K. (2007), Experimental mechanical
995 compaction of clay mineral aggregates - Changes in physical properties of mudstones

during burial, *Marine and Petroleum Geology*, *24*, 289-311, doi:10.1016/j.marpetgeo.2007.03.006.

Moore, J. C., & Saffer, D. (2001), Updip limit of the seismogenic zone beneath the accretionary prism of southwest Japan: an effect of diagenetic to low-grade metamorphic processes and increasing effective stress, *Geology*, *29*(2), 183-186, doi:10.1130/0091-7613(2001)029<0183:ULOTSZ>2.0.CO;2.

Moore, G. F., Taira, A., Klaus, A., Becker, L., Boeckel, B., Cragg, B. A., Dean, A., Fergusson, C. L., Henry, P., Hirano, S., Hisamitsu, T., Hunze, S., Kastner, M., Maltman, A. J., Morgan, J. K., Murakami, Y., Saffer, D. M., Sánchez-Gómez, M., Screaton, E. J., Smith, D. C., Spivack, A. J., Steurer, J., Tobin, H. J., Ujiie, K., Underwood, M. B., & Wilson, M. (2001a), New insights into deformation and fluid flow processes in the Nankai Trough accretionary prism: Results of Ocean Drilling Program Leg 190, *Geochemistry, Geophysics, Geosystems*, *2*(10), doi:10.1029/2001GC000166.

Moore, G. F., Taira, A., Klaus, A., et. Al (2001b), *Proc. ODP, Init. Repts.*, *190*, College Station, TX (Ocean Drilling Program), doi:10.2973/odp.proc.ir.190.2001.

Moore, G. F., et al. (2009), Structural and seismic stratigraphic frameworkof the NanTroSEIZE Stage 1 transect, in *Proc. IODP 314/315/316*, edited by M. Kinoshita, H. Tobin, J. Ashi, G. Kimura, S. E. Lallemand, E. Screaton, D. Curewitz, H. Masago, K. T. Moe and the Expedition Scientists, Integrated Ocean Drilling Program Management International, Inc., Washington, DC, doi:10.2204/iodp.proc.314315316.102.2009.

Neuzil, C. (1994), How permeable are clays and shales?, *Water Resources Research*, *30*(2), 145-150, doi:10.1029/93WR02930.

Obana, K., & Kodaira, S. (2009), Low-frequency tremors associated with reverse faults in a shallow accretionary prism, *Earth Planet. Sci. Lett.*, *287*(1-2), 168-174.

Okino, K., Shimakawa, Y., & Nagaoka, S. (1994), Evolution of the Shikoku Basin, *J. Geomagn. Geoelectr.*, *46*, 463-479.

Park, J.-O., Tsuru, T., No, T., Takizawa, K., Sato, S., & Kaneda, Y. (2008), High-resolution 3D seismic reflection survey and prestack depth imaging in the Nankai Trough off southeast Kii Peninsula, *Butsuri Tansa*, 61, 231-241 (in Japanese with English abstract).

Reece, J. S., Flemings, P. B., Dugan, B., Long, H., & Germaine, J. T. (2012), Permeability-porosity relationships of shallow mudstones in the Ursa Basin, northern deepwater Gulf of Mexico, *Journal of Geophysical Research*, *117*(B12), doi:10.1029/2012JB009438.

Reece, J. S., Flemings, P. B., & Germaine, J. T. (2013), Data report: permeability, compressibility, and microstructure of resedimented mudstone from IODP Expedition 322, Site C0011, in Proceedings of the Integrated Ocean Drilling Program, 322, edited by S. Saito, M. B. Underwood, Y. Kubo and the Expedition Scientists, Tokyo (International Ocean Drilling Program Management International, Inc.), doi:10.2204/iodp.proc.322.205.2013.

1034 Rubey, W. W., & Hubbert, M. K. (1959), Overthrust belt in geosynclinal area of western
1035 Wyoming in light of fluid-pressure hypothesis, 2: Role of fluid pressure in mechanics of
1036 overthrust faulting, *GSA Bulletin, 70*(2), 167-205.

1037 Saffer, D. M., & Bekins, B. A. (1998), Episodic fluid flow in the Nankai accretionary complex;
1038 timescale, geochemistry, flow rates, and fluid budget, *Journal of Geophysical Research*,
1039 *103*(B12), 30,351-330,370, doi:10.1029/98JB01983.

1040 Saffer, D. M., & Bekins, B. A. (2002), Hydrologic controls on the morphology and mechanics of
1041 accretionary wedges, *Geology*, *30*, 271-274.

1042 Saffer, D. M., & Bekins, B. A. (2006), An evaluation of factors influencing pore pressure in
1043 accretionary complexes: Implications for taper angle and wedge mechanics, *J. Geophys.*
1044 *Res.*, *111*, B04101, doi:10.1029/2005JB003990.

1045 Saffer, D. M., & Tobin, H. J. (2011), hydrogeology and mechanics of subduction zone forearcs:
1046 Fluid flow and pore pressure, *Annu. Rev. Earth Planet. Sci.*, *39*, 157-186,
1047 doi:10.1146/annurev-earth-040610-133408.

1048 Saito, S., Underwood, M. B., Kubo, Y., & the Expedition 322 Scientists (2010), *Proc. IODP*,
1049 *322*, Tokyo (Integrated Ocean Drilling Program Management International, Inc.),
1050 doi:10.2204/iodp.proc.322.2010.

1051 Santagata, M. C., & Kang, Y. I. (2007), Effects of geologic time on the initial stiffness of clays,
1052 *Engineering Geology*, *89*, 98-111, doi:10.1016/j.enggeo.2006.09.018.

1053 Scheidegger (1974), *The Physics of Flow Through Porous Media*, 3rd. edn. ed., University of
1054 Toronto Press, Toronto.

1055 Schlömer, S., & Krooss, B. M. (1997), Experimental characterisation of the hydrocarbon sealing
1056 efficiency of cap rocks, *Mar. Petrol. Geol.*, *14*, 563–578.

1057 Schneider, J. (2011), *Compression and permeability behavior of natural mudstones* (Doctoral
1058 dissertation), 321 pp, The University of Texas at Austin, Austin.

1059 Schneider, J., Flemings, P. B., Dugan, B., Long, H., & Germaine, J. T. (2009), Overpressure and
1060 consolidation near the seafloor of Brazos-Trinity Basin IV, Northwest Deepwater Gulf of
1061 Mexico, *J. Geophys. Res.*, *114*(B05102), 13, doi:10.1029/2008JB005922.

1062 Schneider, J., Flemings, P. B., Day-Stirrat, R. J., & Germaine, J. T. (2011), Insights into pore-
1063 scale controls on mudstone permeability through resedimentation experiments, *Geology*,
1064 *39*(11), 1011-1014, doi:10.1130/G32475.1.

1065 Scholz, C.H. (1998), Earthquakes and friction laws, *Nature*, *391*, 37-42.

1066 Schumann, K, Behrmann, J. H., Stipp, M., Yamamoto, Y., Kitamura, Y., & Lempp, C. (2014),
1067 Geotechnical behavior of mudstones from the Shimanto and Boso accretionary

complexes, and implications for the Nankai accretionary prism, *Earth, Planets, and Space*, 66(129), doi:10.1186/1880-5981-66-129.

Screaton, E. J., & Ge, S. (2012), The impact of megasplay faulting and permeability contrasts on Nankai Trough subduction zone pore pressures, *Geophysical Research Letters, 39*(22), doi:10.1029/2012GL053595.

Seno, T., Stein, S., & Gripp, A. E. (1993), A model for the motion of the Philippine Sea Plate consistent with NUVEL-1 and geological data, *Journal of Geophysical Research, 98*(B10), 17941-17948, doi:10.1029/93JB00782.

Sheahan, T. C. (1991), *An experimental study of the time-dependent undrained shear behavior of resedimented clay using automated stress path triaxial equipment* (Doctoral dissertation), 952 pp, Massachusetts Institute of Technology, Cambridge.

Skarbek, R. M., & Saffer, D. M. (2009), Pore pressure development beneath the décollement at the Nankai subduction zone: Implications for plate boundary fault strength and sediment dewatering, *J. Geophys. Res., 114*(B07401), doi:10.1029/2008JB006205.

Skempton, A. W. (1970), The consolidation of clays by gravitational compaction, *Journal of the Geological Society London, 125*, 373-411.

Skempton, A.W., & Jones, O.T. (1944), Notes on the compressibility of clays, *Q. J. Geol. Soc., 100*, 119-135, doi:10.1144/GSL.JGS.1944.100.01-04.08.

Spinelli, G. A., Giambalvo, E. R., & Fisher, A. T. (2004), *Sediment permeability, distribution, and influence on fluxes in oceanic basement, in Hydrogeology of the Oceanic Lithosphere*, edited by E. E. Davis and H. Elderfield, p. 706, Cambridge University Press, Cambridge.

Suppe, J. (2007), Absolute fault and crustal strength from wedge tapers, *Geology, 35*(12), 1127, doi:10.1130/g24053a.1.

Tavenas, F., Jean, P., Leblond, P., & Leroueil, S. (1983), The permeability of natural soft clays, Part 2: Permeability characteristics, *Canadian Geotechnical Journal, 20*, 645-660, doi:10.1139/t83-073.

Taylor, D.W. (1942), Research on consolidation of clays, Serial 82, Massachusetts Institute of Technology, Cambridge, MA.

Tobin, H. J., Kinoshita, M., Ashi, J., Lallemant, S., Kimura, G., Screaton, E., Thu, M. K., Masago, H., Curewitz, D., & Expedition Scientists (2009), NanTroSEIZE Stage 1 expeditions: introduction and synthesis of key results, *Proc. IODP, 314/315/316*, doi:10.2204/iodp.proc314315316.101.2009.

Tobin, H., Hirose, T., Ikari, M., Kanagawa, K., Kimura, G., Kinoshita, M., Kitajima, H., Saffer, D., Yamaguchi, A., Eguchi, N., Maeda, L., Toczko, S., & the Expedition 358 Scientists

(2020), Expedition 358 Summary, *Proceedings of the International Ocean Discovery Program*, *358*, doi:10.14379/iodp.proc.358.101.2020.

Underwood, M.B. (2007), *Sediment inputs to subduction zones: Why lithostratigraphy and clay mineralogy matter*. In The Seismogenic Zone of Subduction Thrust Faults, pp. 42-85, New York, NY, Columbia University Press, doi:10.7312/dixo13866-003.

Underwood, M. B., Saito, S., Kubo, Y., & the Expedition 322 Scientists (2010a), IODP Expedition 322 drills two sites to document inputs to the Nankai Trough subduction zone, *Scientific Drilling*, *10*, 14-25, doi:10.2204/iodp.sd.10.02.2010.

Underwood, M. B., Saito, S., Kubo, Y., & the Expedition 322 Scientists (2010b), Expedition 322 summary. In Saito, S., Underwood, M.B., Kubo, Y., and the Expedition 322 Scientists, *Proc. IODP*, *322*, Tokyo (Integrated Ocean Drilling Program Management International, Inc.), doi:10.2204/iodp.proc.322.101.2010.

Underwood, M. B., & Guo, J. (2013), Data report: clay mineral assemblages in the Shikoku Basin, NanTroSEIZE subduction inputs, IODP Sites C0011 and C0012. *In* Saito, S., Underwood, M.B., Kubo, Y., and the Expedition 322 Scientists, *Proc. IODP*, 322, Tokyo (Integrated Ocean Drilling Program Management International, Inc.), doi:10.2204/iodp.proc.322.202.2013.

Vrolijk, P. (1990), On the mechanical role of smectite in subduction zones, *Geology*, *18*, 703-707.

Wang, K. (1994), Kinematic models of dewatering accretionary prisms, *J. Geophs. Res.*, *99*(B3), 4429-4438, doi:10.1029/93JB03366.

Wood, D. M. (1990), *Soil behavior and critical state soil mechanics*, 462 pp., Cambridge Univ. Press, New York.

Yang, Y. L., & Aplin, A. C. (2004), Definition and practical application of mudstone porosity-effective stress relationships, *Petroleum Geoscience*, *10*(2), 153-162.

Yang, Y. L., & Aplin, A. C. (2007), Permeability and petrophysical properties of 30 natural mudstones, *Journal of Geophysical Research*, *112*(B03206), doi:10.1029/2005JB004243.

Yang, Y., & Aplin, A. C. (2010), A permeability-porosity relationship for mudstones, *Marine and Petroleum Geology*, *27*(8), 1692-1697, doi:10.1016/j.marpetgeo.2009.07.001.

Table 2. Consolidation Results from Resedimentation and Constant Rate of Strain (CRS) Consolidation Tests of Nankai Mudstone – Silt Mixtures.

			Measured								Fitted			
			Resedimentation		CRS						$\ln(v)$ vs. $\ln(\sigma'_v)$			
Nankai mudstone [%]	Silt [%]	cf_v	e_0 at 1 kPa	C_C [a] [MPa^{-1}]	P'_c [MPa]	e_0 at 1 MPa	C_C [b] [MPa^{-1}]	C_C [c] [MPa^{-1}]	C_C [d] [MPa^{-1}]	C_e [MPa^{-1}]	$\ln(1+e_0)$	v_0	C	R^2
100	0	0.56	2.77	-0.62	0.117	0.96	0.66	0.48	0.36	-0.07	0.671	1.968	-0.116	0.9972
88	12	0.50	2.63	-0.60	0.091	0.86	0.56	0.43	0.32	-0.06	0.620	1.869	-0.108	0.9981
76	24	0.48	2.44	-0.57	0.115	0.79	0.50	0.39	0.31	-0.06	0.581	1.797	-0.102	0.9989
64	36	0.41	2.11	-0.47	0.109	0.69	0.43	0.34	0.29	-0.04	0.525	1.699	-0.094	0.9991
52	48	0.36	1.80	-0.38	0.108	0.68	0.34	0.29	0.27	-0.03	0.518	1.681	-0.082	0.9997
40	60	0.32	1.72	-0.37	0.100	0.67	0.25	0.24	0.24	-0.04	0.514	1.669	-0.069	0.9981

Note. Silt = silt-size silica (US MIN U SIL 40 purchased from US Silica). cf_v = volumetric clay fraction rounded to two digits after the decimal point, CRS = constant rate of strain consolidation test. e_0 = reference void ratio at 1 kPa (resedimentation) or 1 MPa (CRS). C_c = compression index. C_e = expansion index. $v_0 = (1+e_0)$ = specific volume at a vertical effective stress of unity (1 MPa). C = compression index in log-log space of void ratio and effective stress. R^2 = coefficient of determination. [a] constrained over 2.6 – 100 kPa. [b] constrained over 0.2 – 1 MPa. [c] constrained over 1 – 5 MPa. [d] constrained over 5 – 20 MPa.